Journal of
METAMORPHIC GEOLOGY

J. metamorphic Geol., 2015, **33,** 1003–1024 doi:10.1111/jmg.12166

LP/HT metamorphism as a temporal marker of change of deformation style within the Late Palaeozoic accretionary wedge of central Chile

T. HYPPOLITO,[1,2] C. JULIANI,[1] A. GARCIA-CASCO,[2,3] V. MEIRA,[1] A. BUSTAMANTE[4] AND C. HALL[5]
[1]*Departamento de Geoquímica e Geotectônica, Instituto de Geociências, Universidade de São Paulo, Rua do Lago 562, CEP 05508-080, São Paulo, SP, Brazil (thahyppolito@gmail.com)*
[2]*Departamento de Mineralogía y Petrología, Universidad de Granada, Avda. Fuentenueva SN, 18002 Granada, Spain*
[3]*Instituto Andaluz de Ciencias de la Tierra (CSIC-UGR), Avda. de las Palmeras 4, E-18100 Armilla, Granada, Spain*
[4]*Departamento de Geologia, Universidade Federal de Pernambuco, Rua Acadêmico Hélio Ramos Várzea 50740530, Recife, PE, Brazil*
[5]*Argon Geochronology Laboratory, University of Michigan, 2534 C.C. Little Building, 1100 North University Avenue, Ann Arbor, MI 48109-1005, USA*

ABSTRACT A Late Palaeozoic accretionary prism, formed at the southwestern margin of Gondwana from Early Carboniferous to Late Triassic, comprises the Coastal Accretionary Complex of central Chile (34–41°S). This fossil accretionary system is made up of two parallel contemporaneous metamorphic belts: a high-pressure/low temperature belt (HP/LT – Western Series) and a low pressure/high temperature belt (LP/HT – Eastern Series). However, the timing of deformation events associated with the growth of the accretionary prism (successive frontal accretion and basal underplating) and the development of the LP/HT metamorphism in the shallower levels of the wedge are not continuously observed along this paired metamorphic belt, suggesting the former existence of local perturbations in the subduction regime. In the Pichilemu region, a well-preserved segment of the paired metamorphic belt allows a first order correlation between the metamorphic and deformational evolution of the deep accreted slices of oceanic crust (blueschists and HP greenschists from the Western Series) and deformation at the shallower levels of the wedge (the Eastern Series). LP/HT mineral assemblages grew in response to arc-related granitic intrusions, and porphyroblasts constitute time markers recording the evolution of deformation within shallow wedge material. Integrated *P–T–t–d* analysis reveals that the LP/HT belt is formed between the stages of frontal accretion (D_1) and basal underplating of basic rocks (D_2) forming blueschists at *c*. 300 Ma. A timeline evolution relating the formation of blueschists and the formation and deformation of LP/HT mineral assemblages at shallower levels, combined with published geochronological/thermobarometric/geochemistry data suggests a cause–effect relation between the basal accretion of basic rocks and the deformation of the shallower LP/HT belt. The S_2 foliation that formed during basal accretion initiated near the base of the accretionary wedge at ~30 km depth at *c*. 308 Ma. Later, the S_2 foliation developed at *c*. 300 Ma and ~15 km depth shortly after the emplacement of the granitoids and formation of the (LP/HT) peak metamorphic mineral assemblages. This shallow deformation may reflect a perturbation in the long-term subduction dynamics (e.g. entrance of a seamount), which would in turn have contributed to the coeval exhumation of the nearby blueschists at *c*. 300 Ma. Finally, ^{40}Ar–^{39}Ar cooling ages reveal that foliated LP/HT rocks were already at ~350 °C at *c*. 292 Ma, indicating a rapid cooling for this metamorphic system.

Key words: accretionary prism; central Chile; paired metamorphic belt; *P–T–t–d* path.

INTRODUCTION

The temporal and spatial relationships of thermal and mechanical processes in orogens have been a topic of debate for the past 40 years. Our understanding of accretionary wedge dynamics remains incomplete. More specifically the relation between the two main geodynamic processes, namely (i) the formation of thermally-contrasted (pene-) contemporaneous metamorphic belts (*sensu* Miyashiro, 1961; Maruyama, 1997; and revisited by Brown, 2009, 2010, 2014; Maruyama *et al.*, 2010) and (ii) the development of diverse deformational fabrics under the thermally contrasted environments (Platt, 1986; Maruyama, 1997; Feehan & Brandon, 1999; Ring *et al.*, 1999; Gray & Foster, 2004; Richter *et al.*, 2007). In paired metamorphic sys-

tems, the outer (oceanic) part of the accretionary prism evolves under cold thermal gradients that generate high-pressure/low-temperature (HP/LT) metamorphism, while the hinterland regions are typically associated with granitic (*s.l.*) intrusions and development of low-pressure/high-temperature (LP/HT) metamorphism (e.g. Isozaki, 1996, 1997; Brown, 2010; Isozaki *et al.*, 2010 and references therein). During wedge growth at active plate margin settings, the mechanical response to forces acting under these different thermal gradients includes the development of contrasting foliations (e.g. sub-horizontal *v.* sub-vertical) and fabrics (e.g. symmetrical flattening *v.* non-coaxial deformation), large-scale thrust-nappes, shear zones, and vertical faulting, which can affect gradually accreted rock assemblages at different depths in the wedge (Cloos, 1982; Platt, 1986, 1993; Cloos & Shreve, 1988; Isozaki, 1997; Feehan & Brandon, 1999; Ring & Brandon, 1999; Ring *et al.*, 1999; Gray & Foster, 2004; Glodny *et al.*, 2005, 2008; Willner, 2005; Richter *et al.*, 2007 and references therein; Willner *et al.*, 2009, 2012; Angiboust *et al.*, 2014). In spite of such complex dynamics much of our understanding of the tectonic evolution of deep and shallow levels of the accretionary prism stems from the determination of pressure–temperature–deformation–time (*P–T–d–t*) paths and their correlation with deformation episodes (Feehan & Brandon, 1999; Ring & Brandon, 1999; Willner, 2005; Richter *et al.*, 2007).

The Palaeozoic accretionary complex of central Chile (Fig. 1) exhibits a *c.* 300 Ma paired metamorphic belt comprising two contrasting lithological/structural/metamorphic series (González-Bonorino & Aguirre, 1970; González-Bonorino, 1971; Aguirre *et al.*, 1972; Hervé *et al.*, 1984; Willner, 2005; Willner *et al.*, 2005; Richter *et al.*, 2007; Hervé *et al.*, 2013; Hyppolito *et al.*, 2014b). The Western Series comprises strongly deformed oceanic-derived HP/LT units made of metabasic and metasedimentary rocks related to abyssal and trench environments (Willner, 2005; Hyppolito *et al.*, 2014a,b), whereas the Eastern Series is formed by trench-to-forearc metasedimentary rocks that are less deformed and were metamorphosed at shallower levels of the accretionary wedge (Hervé *et al.*, 1984; Hervé, 1988; Willner, 2005). The latter records the thermal effects of subduction-related granitic magmatism that intruded the wedge (Willner, 2005; Richter *et al.*, 2007) and triggered the LP/HT metamorphism (González-Bonorino, 1971; Aguirre *et al.*, 1972; Willner, 2005). Both series have been characterized as a continuous tectonic section within an accretionary wedge that grew under two successive modes of accretion (Richter *et al.*, 2007). The progressive structural evolution between the two series and the change in the deformation style from the Eastern to the Western Series (cf. Hervé, 1988; Richter *et al.*, 2007) has been related to contrasting tectonic regimes prevailing at different portions of a single wedge (Glodny *et al.*, 2005), and by the ongoing change in the mode of accretion from frontal to basal underplating (Willner, 2005; Willner *et al.*, 2005; Richter *et al.*, 2007; Massonne & Willner, 2008).

Recently, considerable progress has been made in determining the structural configuration and thermal-tectonic evolution of the Chilean accretionary wedge, including (i) the characterization of contrasted fabrics in the Western and Eastern Series (Glodny *et al.*, 2005; Richter *et al.*, 2007), (ii) the correlation of *P–T* regime and structural position within the wedge (Willner, 2005), and (iii) the definition of metamorphic-time relations in both series (Willner *et al.*, 2005), and a thermodynamic modelling approach has also been applied to explain the changes in accretion mode within the wedge over time (Massonne & Willner, 2008). In spite of this progress, local-scale observations of the Chilean accretionary prism might provide additional clues about the geodynamic processes that took place along this active plate margin. In this context, the tectonic evolution of this paired belt was investigated by analyzing the temporal relationships between the growth of porphyroblasts in the LP/HT belt and the development of different deformational stages observed in the wedge. Thus, we evaluate how the low strain LP/HT series was affected by basal accretion processes and exhumation-related deformation.

To address these questions, we characterize the evolution of metamorphic history and deformation of greenschist to amphibolite facies rocks associated with the late Palaeozoic granitic intrusions in the Pichilemu region, central Chile (Fig. 2). This region comprises an unusual occurrence of the paired metamorphic system, which is formed by a metasedimentary-rich HP segment that includes only rare ocean-derived lenses (blueschists and HP greenschists) that are sub-parallel to the isograds in the well-developed LP/HT belt (Willner, 2005; Figs 1 & 2). The occurrence of metabasic rocks in the HP belt might provide first-order evidence to decipher the nature of the subducted oceanic crust and its influence on the development of the active margin, e.g. whether seamounts or bathymetric highs were present on the subducted oceanic plate (Willner, 2005; Hyppolito *et al.*, 2014a; Halama & Konrad-Schmolke, 2015). Here we present field/microstructural information recorded by garnet, biotite, chlorite, staurolite and andalusite porphyroblasts, new thermodynamic modelling, and ^{40}Ar–^{39}Ar ages of muscovite and biotite. These results were combined to derive *P–T–t–d* paths in order to understand the dynamic and thermal evolution of the LP/HT metamorphic rocks in the tectonic framework of an accretionary prism (Willner, 2005; Willner *et al.*, 2005; Richter *et al.*, 2007). This work demonstrates how porphyroblasts formed at shallower levels of the wedge during LP/HT metamorphism can shed light on the geodynamic evolution of a paired metamorphic system when

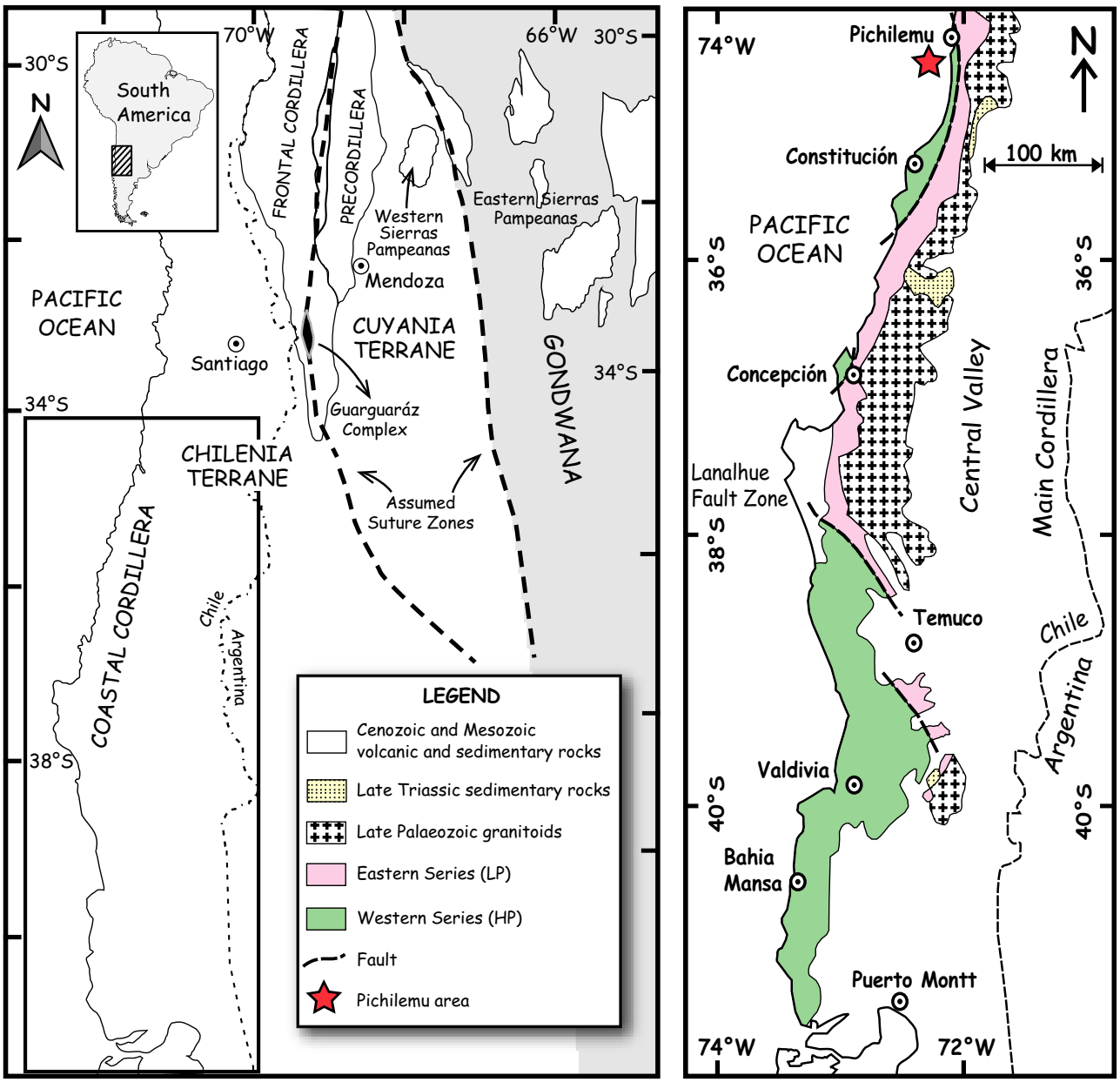

Fig. 1. Geological maps of central Chile to show the location of the Pichilemu area in the Palaeozoic paired metamorphic belt, which comprises the Western and the Eastern Series and Late Palaeozoic granitoids of the Coastal Batholith. Modified after Willner (2005), and Willner *et al.* (2004, 2009).

coupled to a study of the temporal and deformation relationships at various depths in the accretionary prism.

GEOLOGICAL SETTING

The Late Palaeozoic Coastal Cordillera

The metamorphic basement in the Coastal Cordillera, which forms an almost continuous metamorphic belt extending from 32°S to 54°S, includes a Palaeozoic accretionary prism belonging to the circum-Pacific orogen located along the southwestern margin of Gondwana (González-Bonorino & Aguirre, 1970; González-Bonorino, 1971; Aguirre *et al.*, 1972; Ernst, 1975; Hervé *et al.*, 1984; Willner *et al.*, 2001, 2005, 2012; Glodny *et al.*, 2005; Willner, 2005; Hervé *et al.*, 2013, 2014). In the 1970s, this basement was described as a paired metamorphic belt *sensu* Miyashiro (1961) by Aguirre *et al.* (1972). The Western HP/LT and the Eastern LP/HT series represent parallel and coeval metamorphic belts oriented N–S (Figs 1 & 2; Willner, 2005; Willner *et al.*, 2005).

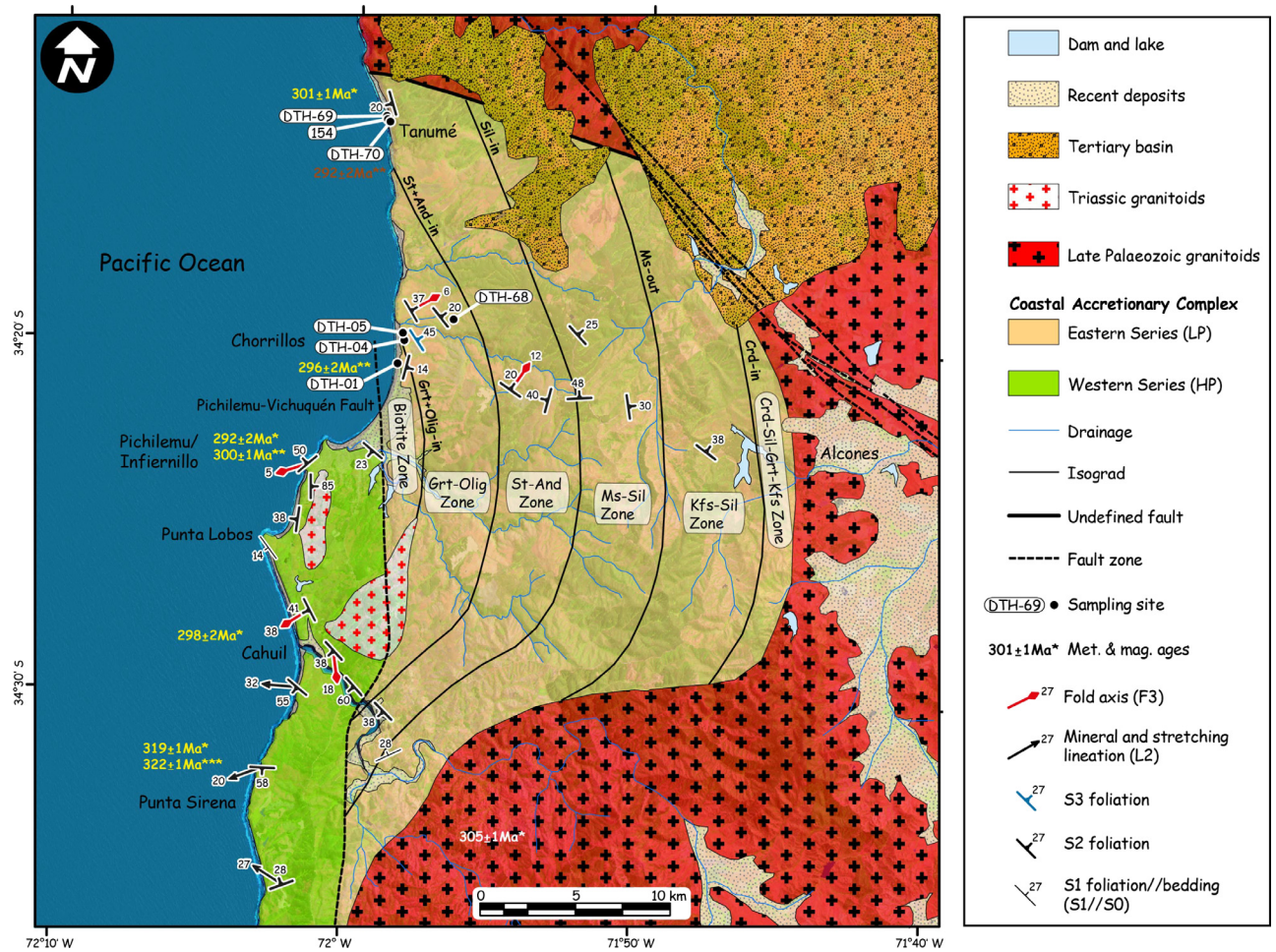

Fig. 2. Geological map of the metamorphic zones in the Pichilemu region (after González-Bonorino, 1971, Hervé *et al.*, 1984; Willner, 2005) with sample locations in the Tanumé and Chorrillos areas. ^{40}Ar–^{39}Ar metamorphic ages are shown in yellow (white mica) and brown (biotite) and are labelled as follows: one star, from Willner *et al.* (2005); two stars, from this study; and three stars, from Hyppolito *et al.* (2014b). The main magmatic activity was dated by Willner *et al.* (2005) and is represented by the age in white (U–Pb zircon evaporation age). Mineral abbreviations follow Whitney & Evans (2010), with Olig, oligoclase.

The (LP/HT) Eastern Series includes psammo-pelitic sequences that represent post-Devonian trench-fill sediments (Hervé, 1988; Willner *et al.*, 2005, 2008; Richter *et al.*, 2007; Hervé *et al.*, 2013) and sedimentary rocks of likely Devonian age from a pre-Carboniferous passive margin (e.g. Hervé, 1988; Glodny *et al.*, 2008) both off scraped against the continental buttress during the earliest stages of Carboniferous accretion at an active plate margin developed at the rear (West) of the Chilenia terrane (Willner *et al.*, 2008, 2011). Throughout the development of the accretionary wedge, the Eastern Series was intruded by granitic rocks (granodiorite, tonalite, granite) of the Coastal Batholith between *c.* 330 and *c.* 300 Ma, with the main activity in central Chile occurring at *c.* 305 Ma (Willner *et al.*, 2005; Hervé *et al.*, 2013, 2014), which caused extensive metamorphic overprinting of the very low grade accretion-related metamorphism (Willner, 2005; Willner *et al.*, 2001). On the other hand, the subduction-related (HP/LT) Western Series is composed of continental-derived rocks (pelites and psammites) formed in abyssal, trench and passive margin settings that are associated with rare ocean-derived rocks now present as greenschist, blueschist, amphibolite and garnet amphibolite (Hervé *et al.*, 1984; Hervé, 1988; Willner, 2005; Hyppolito *et al.*, 2014a). The ocean-derived metabasites include OIB, E-MORB and N-MORB types (Kato, 1985; Hervé, 1988; Kato & Godoy, 1995; Hyppolito *et al.*, 2014a) thought to have formed in a plume–ridge interaction setting (Hyppolito *et al.*, 2014a). It is likely that fragments of seamounts were accreted against the active margin during Palaeozoic subduction (Willner, 2005; Hyppolito *et al.*, 2014a). The metasedimentary and metabasic rocks are intercalated up to the decametre scale, with metabasites forming lenses of up to kilometre in length due to the tectonics of early basal accretion (Willner, 2005; Willner *et al.*, 2009).

The contact between the Western and Eastern Series has been a matter of debate (Ernst, 1975; Hervé, 1988; Glodny *et al*., 2006, 2008; Richter *et al*., 2007; Willner *et al*., 2009). At issue is whether the two series were juxtaposed by a major tectonic discontinuity or whether they belong to a single growing wedge (cf. Glodny *et al*., 2005; Richter *et al*., 2007). Recently, in central Chile Richter *et al*. (2007) proposed that the two series comprise a continuous structural section with deformation increasing to the west (see also Hervé, 1988). For Massonne & Willner (2008) such a gradational change is related to the decreasing geothermal gradient in the subduction system (discussed further below). They proposed a cause/effect relation between the depth of maximum dehydration reactions that soften sedimentary rocks and oceanic crust triggering detachment and accretion of sedimentary and oceanic material at different depths under very low- to low-grade conditions. Willner *et al*. (2009) interpreted reverse faults with an oblique component located along the contact between the two series, such as the Pichilemu–Vichuquen Fault (Figs 1 & 2), to be related to deformation of the accretionary wedge *c*. 100 Ma later during the post-accretionary stage, supporting the transitional nature for the contact.

Mineral zones, mineral assemblages and porphyroblast relations at the Eastern Series

In the Pichilemu region, the metamorphic zonation towards the batholith includes mineral assemblages of the greenschist (biotite zone), amphibolite (staurolite–andalusite and sillimanite zones) and granulite (garnet–cordierite zone) facies, with curved mineral isograds that are oriented approximately N–S (Fig. 2; González-Bonorino & Aguirre, 1970; González-Bonorino, 1971; Aguirre *et al*., 1972; Gana & Hervé, 1983; Hervé *et al*., 1984; Willner, 2005). A summary of mineral zones and facies is given in Table 1.

The biotite zone is characterized by the coexistence of biotite + chlorite ± garnet, and the staurolite–andalusite zone is essentially defined by the assemblages garnet + biotite, garnet + biotite + staurolite, biotite + staurolite + andalusite (cf. Aguirre *et al*., 1972; Willner, 2005). The muscovite–sillimanite zone is

Table 1. Summary of mineral zones and metamorphic facies in central Chile; compiled from González-Bonorino & Aguirre (1970), Aguirre *et al*. (1972), Hervé *et al*. (1984), Willner (2005) and this work.

Mineral Zone/ Met. Facies Conditions	Chl-Bt/ Greenschist	Grt-Olig/ Greenschist-Amphibolite	And[a], St-Grt[a], St-And/ Amphibolite	Sil-I[a], Sil[a], Ms-Sil/ Amphibolite	Sil-II[a], Sil-Crd-Grt-Kfs[a], Kfs-Sil/ Granulite
Quartz	----------	----------	----------	----------	----------
Albite	----------				
Plagioclase		----------	----------	----------	----------
K-feldspar					----------
Chlorite	----------	----------			
Muscovite	----------	----------	----------	----------	
Biotite	----------	----------	----------	----------	----------
Chloritoid			-----		
Staurolite			----------		
Andalusite[b]		---	----------	----	
Cordierite			-----	----------	----------
Sillimanite[b]				----------	----------
Garnet	---	----------	----------	----------	----------
Cummingtonite[c]			----------		
Clinopyroxene[c]				--	----------
Orthopyroxene[c]					----------

[a]Different denominations for similar metamorphic zones given by Aguirre *et al*. (1972) and Willner (2005), respectively. In this study we denote this zone as 'St–And' due to the occurrence of both minerals in the outer zone of the LP/HT belt. We propose 'Ms–Sil' and 'Kfs–Sil' zones in this study (see text for clarification).
[b]To the south of Pichilemu region, the absence of staurolite and the coexistence of these two polymorphs in medium-grade condition rocks led Willner (2005) to define the 'andalusite–sillimanite zone'.
[c]Rare occurrences described at the Eastern Series (cf. Aguirre *et al*., 1972).

characterized by the coexistence of sillimanite + garnet ± cordierite ± andalusite (Aguirre *et al.*, 1972; Willner, 2005) (Fig. 2). The breakdown of muscovite and appearance of K-feldspar (+cordierite) define the sillimanite subzone II of Aguirre *et al.* (1972), the cordierite–sillimanite–garnet–K-feldspar zone of González-Bonorino (1971) and Willner (2005), or the K-feldspar–sillimanite zone (this study). A narrow zone characterized by the appearance of oligoclase and garnet is observed between the biotite and staurolite–andalusite zones (Fig. 2; González-Bonorino, 1971; Hervé *et al.*, 1984). In this study we maintain the delimitation of this intermediate zone and present, for the first time, *P–T* estimates for these rocks.

Complex mineral growth and deformation relationships characterize the porphyroblasts formed during the LP/HT metamorphism. Hervé *et al.* (1984) pointed out that the internal foliation recorded within staurolite porphyroblasts in the staurolite–andalusite zone in the Tanumé region differs from the external S_2 foliation that wraps around them. On the other hand, Willner (2005) considered staurolite and andalusite porphyroblasts to be essentially post-kinematic with respect to both the S_1 and S_2 foliations, and interpreted the local rotation of porphyroblasts within S_2 as evidence of waning deformation after the thermal overprint under the same stress field that prevailed before intrusion of the arc-related magmas. Willner *et al.* (2009) interpreted biotite, andalusite and staurolite as static post-S_2 porphyroblasts that may be elongated parallel to the regional lineation L_2, and proposed that the Eastern Series was affected by D_2 deformation during and after the high-*T* metamorphism, reflecting the effects of deformational due to basal underplating. Further to the south of the studied area (38°S), Glodny *et al.* (2008) described andalusite as syn-to-post-S_1, and staurolite and biotite porphyroblasts as pre-dating S_2. Hervé (1977) had already described syn- to post-S_2 andalusite and garnet porphyroblasts in the same area. Combining petrological and geochronological data, Glodny *et al.* (2008) interpreted the arc magmas to have intruded the Eastern Series at 306–290 Ma, during D_2 deformation at the rear of the wedge. Close to this region (38–41°S), Martin *et al.* (1999) described LP/HT-related minerals (andalusite, sillimanite, cordierite) as pre- to syn-S_1. Such interpretations highlight the complex tectonic-thermal history along the fossil accretionary margin during the forearc evolution.

Previous *P–T* estimates

Willner (2005) provided thermobarometric results for samples distributed along the Eastern Series in central Chile (34–35°30′S) and a petrogenetic grid appropriate to the *P–T* conditions of the lower and higher grade zones, suggesting similar peak pressures of 3.0 ± 0.5 kbar during the thermal overprint. Using the multiequilibrium method of Berman (1988), Willner (2005) calculated *P–T* of 2–3 kbar and 400–450 °C for the biotite zone using the assemblage biotite–chlorite–muscovite–quartz and assuming K-feldspar present (i.e. not present in the assemblage but used in the calculations). For the staurolite–andalusite zone, *P–T* was estimated at 2.5–3 kbar and 520–580 °C in garnet–staurolite–biotite rocks based on the petrogentic grid of Spear & Cheney (1989) and 3.2 kbar and 555 °C using the multiequilibrium method of Berman (1988) applied to coexisting plagioclase, garnet and biotite. Temperatures for the assemblage cordierite–biotite–garnet–sillimanite–plagioclase–quartz were estimated at 650–720 °C and 2.5–3.5 kbar by combining multivariant reactions and exchange thermometry (Willner, 2005). The breakdown of muscovite + quartz at temperature below the wet granite solidus indicates pressures lower than 3.6 kbar (Willner, 2005).

Importantly, Willner *et al.* (2000) showed that in areas where the Eastern Series was not affected by the arc-related thermal overprint (e.g. the Chonos archipelago, 44–46°S), the *P–T* conditions indicate very-low grade metamorphism of the pumpellyte–actinolite facies (~5.5 kbar and 250–280 °C). In this study the earlier low-grade regional metamorphism is interpreted to be related to frontal accretion (M1) as opposed to the thermal overprint that formed the LP/HT metamorphic belt (M2).

Structural features, modes of growth and geodynamic model for wedge evolution

Major systematic differences between the Western and Eastern Series include: (i) structural position within the accretionary wedge, (ii) internal fabric, and (iii) predominant constituent lithologies (Hervé *et al.*, 1984; Kato, 1985; Hervé, 1988; Glodny *et al.*, 2005, 2008; Willner, 2005; Richter *et al.*, 2007). The actual geodynamic model proposed to explain such contrasting features recognizes that frontal and basal modes of accretion occurred successively (Willner, 2005; Richter *et al.*, 2007) and led to the vertical growth of the wedge during *c.* 100 Ma of subduction (from *c.* 320 to *c.* 224 Ma; Willner *et al.*, 2005). This model is based on the flow-field concept of Feehan & Brandon (1999) and Ring & Brandon (1999), which describe how material moving within a wedge is affected by different modes of accretion and how this culminates in the observed architecture and internal fabrics. The material progressively transferred to the growing wedge is balanced by erosion at the top affecting the resulting mode of accretion. If underplating (i.e. imbrication of oceanic and sedimentary material at the base of the wedge) does not occur, deformation is concentrated at the shallower levels of the prism and is dominated by horizontal shortening of offscraped units, when a thickening flow field prevails (Richter *et al.*, 2007). On the other hand, basal accretion enhances the formation of topographic elevations (and hence erosion)

triggering the formation of a more active and erosive system, and vertical shortening develops due to a thinning flow field. In the Chilean accretionary wedge, the thickening flow field accounts for horizontal shortening of rocks forming the Eastern Series, as revealed by the vertical S_1 foliation related to the F_1 folds. On the other hand, the ensuing basal accretion is evidenced by the transposition of the S_1 foliation by a sub-horizontal and penetrative S_2 foliation (locally S_3; Richter *et al*., 2007).

Richter *et al*. (2007) proposed that the timing of change from frontal to basal accretion modes occurred at *c*. 300 Ma (metamorphic peak ages of the Western Series estimated by means of ^{40}Ar–^{39}Ar dating of phengite from blueschists at the Pichilemu region; Willner *et al*., 2005). More recently, an age of *c*. 308 Ma was suggested for the change of the accretion mode, based on the youngest detrital zircon ages from the accreted metasedimentary rocks (Willner *et al*., 2008), also corroborated by ^{40}Ar–^{39}Ar ages in white mica (Willner *et al*., 2005; Hyppolito *et al*., 2014b). Willner *et al*. (2005) indicated that the LP/HT metamorphism in central Chile formed at 301–296 Ma (^{40}Ar–^{39}Ar ages of muscovite from the Pichilemu region and further south), in response to the main magmatic arc activity in this region at *c*. 305 Ma (Pb/Pb evaporation age of zircon from granite; Willner *et al*., 2005), during the early stages of accretion at the base of the wedge. Considering the transitional nature of the structural contact, Richter *et al*. (2007) suggested that changing from frontal to basal accretion was a gradual and not an abrupt process in time. However the paucity of field evidence precluded testing this assumption.

Based on pseudosection calculations for metabasite and psammo-pelite compositions, Massonne & Willner (2008) related the systematic change in the accretionary mode to the continuous cooling of the subduction system. Due to decreasing temperature, significant dehydration (and softening of the wedge rocks) might occur at higher pressure conditions, resulting in deeper underplating (i.e. basal accretion; Massonne & Willner, 2008). Even though this approach provides an explanation for the gradual change in mode of accretion, the particular effects of basal accretion on the early accreted Eastern Series cannot be explained by cooling of the subduction system alone, suggesting that tectonic/mechanical processes also controlled the strain distribution within the wedge, as discussed below.

LITHOLOGY AND FIELD RELATIONS IN THE PICHILEMU REGION

Greenschist and transitional amphibolite facies zones (Chorrillos area)

Metric sequences of gray to brownish phyllites, alternating with centimetre- to decimetre-sized quartz- and mica-rich layers, comprise the lithological varieties along a few kilometres at the coastal zone of Chorrillos (Figs 2 & 3). The structure is characterized by a sub-horizontal transposition foliation S_2, in which the S_1 foliation is preserved as intrafolial folds (Fig. 3a). In highly deformed domains, the S_2 foliation is deformed by a crenulation cleavage S_3 that locally transposes the second foliation (Fig. 3b,c), pointing to continuous deformation, but remnants of the S_1 are still recognized (Fig. 3c). Greenschist facies metamorphism is characterized by the mineral assemblage chlorite–biotite–muscovite–quartz–plagioclase–ilmenite defining the biotite zone. Scarce fine-grained garnet marks the appearance of the garnet–oligoclase zone indicating transitional metamorphic conditions between the greenschist and amphibolite facies. Quartz veins are widespread and form intrafolial F_2 folds locally refolded by F_3 folds. In the oligoclase–garnet zone fine grained biotite ± andalusite occur within quartz veins folded by F_2 folds.

Amphibolite facies zone (Tanumé area)

Quartz-micaschists (±andalusite, garnet and staurolite) and garnet-bearing psammites are the dominant lithotypes outcropping continuously for kilometres along the coast at Tanumé (Fig. 3d). The pelites and psammites are intercalated at the centimetre-scale forming metric-scale sequences. Calc-silicate rocks occur as rare lenses within the sequence (Hervé *et al*., 1984). The structure is characterized by a sub-horizontal penetrative S_2 foliation (Fig. S1a) but, locally, the main foliation in dominant quartz- and feldspar-rich packages is the S_1 foliation and primary sedimentary structures such as cross stratification are still observed. Abundant quartz (±andalusite) veins occur and are isoclinally folded by F_2 folds (Fig. 3d–f). Medium-grade conditions are represented by the assemblages biotite–andalusite–staurolite–muscovite–quartz–plagioclase–ilmenite and biotite–garnet–quartz–plagioclase–ilmenite ± staurolite ± muscovite.

A prominent feature of these rocks is the presence of chiastolitic andalusite porphyroblasts of up to 25 cm of length (Figs 3e & S1b). Chiastolitic porphyroblasts show complex growth patterns characterized by randomly oriented grains that were folded, partially broken (Fig. 3e,f), rotated and wrapped (Fig. S1b) during the formation of the S_2 transposition foliation, revealing that andalusite growth preceded the main D_2 event. The presence of andalusite within and at the walls of isoclinally folded quartz veins corroborates this interpretation (Fig. 3e,f).

ANALYTICAL TECHNIQUES

Mineral analyses were obtained by wavelength dispersive spectrometry using a CAMECA SX-100 microprobe analyser [Center of Scientific Facilities (CIC), University of Granada] operated at 15 kV/

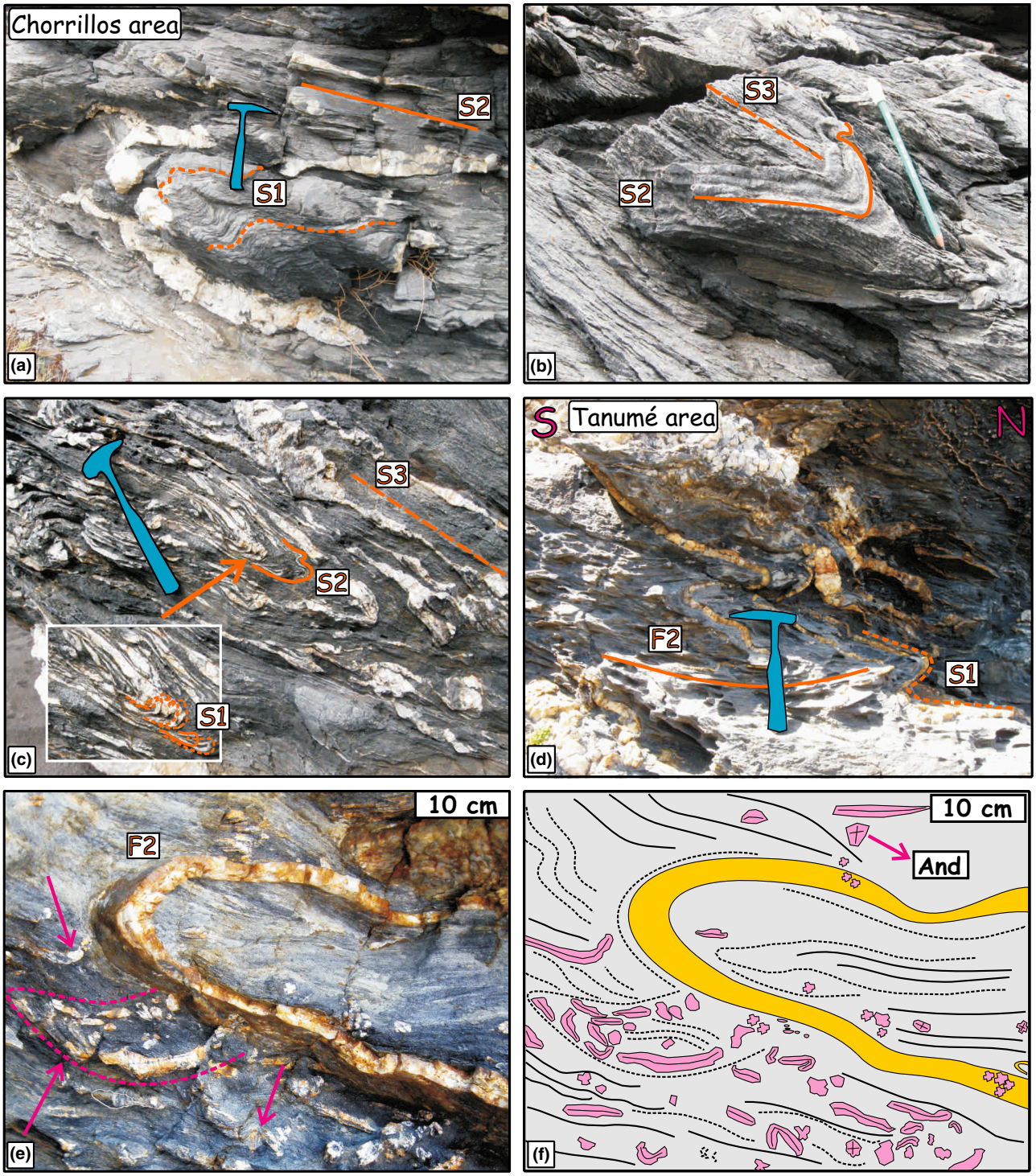

Fig. 3. Field relations in the Chorrillos and Tanumé areas. (a) Transposition foliation S_2 and vestiges of the S_1 foliation preserved as intrafolial folds at Chorrillos beach. (b) and (c) Highly deformed domains at Chorrilos area with crenulation (F_3) of the S_2 foliation. The inset in (c) shows vestiges of S_1. (d) Transposition of the S_1 foliation by F_2 folding at Tanumé beach, which is highlighted by abundant isoclinally folded quartz veins. (e) and (f) Isoclinally folded quartz veins bearing andalusite in a zone of transposition of the S_1 foliation by S_2.

15 nA beam current with a 5 μm beam diameter. Albite (Na), periclase (Mg), SiO_2 (Si), Al_2O_3 (Al), sanidine (K), Fe_2O_3 (Fe), $MnTiO_3$ (Mn), $BaSO_4$ (Ba), Cr_2O_3 (Cr), diopside (Ca), TiO_2 (Ti) and vanadinite (Cl) were used as calibration standards. Representative analyses are provided in Table S1a–g. Chlorite

and mica compositions were normalized to 28 and 11 oxygen, respectively, assuming $Fe_{total} = Fe^{2+}$. Garnet and ilmenite compositions were normalized to 12 and 3 oxygen, and 8 and 2 cations, respectively, with Fe^{3+} estimated by stoichiometry. Following Holdaway *et al.* (1991, 1995), staurolite compositions were normalized to 48 oxygen, $Si+Al+2/3Ti+Fe^{3+} = 25.55$, and $Fe^{3+} = 3.5\%$ of Fe_{total}. Plagioclase and epidote compositions were normalized to 8 and 12.5 oxygen, respectively, assuming Fe_{total} as Fe^{3+}. Mineral abbreviations follow the scheme of Whitney & Evans (2010). Atoms per formula unit and Mg-number ($Mg/(Mg+Fe^{2+})$) are abbreviated as a.p.f.u. and Mg#, respectively.

Elemental X-ray maps were obtained with the same machine operated at 15 keV and 250 nA, with a focused beam, pixel size of 8 μm and counting time of 30 ms per pixel. The images were processed with software DWImager (R. Torres-Roldán & A. Garcia-Casco, unpublished data) to highlight the minerals and textures of interest. In the images, some minerals were masked out and minerals of interest were overlain onto a grayscale image calculated with the expression $\sum$ (a.p.f.u./nA/s)$i \times Ai$ (where A is the atomic number and i corresponds to Si, Ti, Al, Fe, Mn, Mg, Ca, Na, Ba, K, P, F and Cl) that contains the basic textural information of the scanned areas.

Whole-rock major element (wt%) compositions were determined at the CIC (University of Granada) with a PHILIPS Magix Pro (PW-2440) XRF spectrometer using glass beads made of 0.6 g of powdered sample diluted in 6 g of $Li_2B_4O_7$. The results are listed in Table S2. Mineral and whole-rock composition were plotted in composition phase diagrams after projection from appropriate phases and exchange vectors using software CSpace (Torres-Roldán *et al.*, 2000). Whole-rock compositions of selected samples were used for the calculation of *P–T* pseudosections using the software package PERPLE_X (Connolly, 1990, 2005, version 6.6.8).

$^{40}Ar/^{39}Ar$ analyses of muscovite and biotite were performed at the Argon Geochronology Laboratory of the University of Michigan using a continuous laser for step heating and a VG 1200S noble gas mass spectrometer equipped with a Daly detector operated in analog mode. The mass spectrometer was operated using the methods outlined in Streepey *et al.* (2000) and Keane *et al.* (2006). Samples were packed within pure Al foil packs and irradiated in a medium flux location inside the McMaster Nuclear reactor for 90 MWh within two irradiation packages. Quoted ages are calculated relative to an age of 520.4 Ma for hornblende standard MMHb-1. After irradiation, a small number of grains (between two and four) with 150–250 μm were chosen from each sample for extraction and purification of argon by the step-heating method.

BULK COMPOSITION OF LOW-GRADE METASEDIMENTARY ROCKS FROM THE PICHILEMU REGION

Whole-rock compositions of metasedimentary rocks from the Eastern Series are scarce in the literature. Here 15 new whole-rock analyses of samples from the Chorrillos and Tanumé areas are provided (Table S2).

In Fig. S2, the whole-rock compositions are plotted on the AKF (Al_2O_3–$KAlO_2$–FeO) and AFM (Al_2O_3–FeO–MgO) diagrams projected from the coexisting phases quartz, ilmenite, plagioclase (Ab_{83}, average composition), apatite and H_2O, using the exchange vectors $SiNaAlCa_{-1}$, $MnFe_{-1}$ and $MgFe_{-1}$ (AKF), and quartz, muscovite (Si = 3.09, average composition), plagioclase (Ab_{83}, average), ilmenite, apatite and H_2O, using the exchange vectors $MnFe_{-1}$ and $SiNaAlCa_{-1}$ (AFM), in order to properly condense the compositional space (i.e. so the number of old components equal to the number of new components). The average compositions of plagioclase (varying from albite to andesine) and muscovite (see the AFM diagram) include chemical analyses from rocks belonging to the biotite and staurolite–andalusite zones (greenschist to amphibolite facies). The thermodynamic validity of the projections is not fully accomplished (Greenwood, 1975) because of the use of average compositions and exchange vectors, but the imperfections are minor and the projections are valid for evaluating the variation in bulk-rock composition and its effect on mineral assemblages. As shown in Fig. S2, the samples from greenschist to amphibolite facies zones are pelites (AKF diagram), and have broadly constant Mg# in the range 0.29–0.39 (AFM diagram), with the exception of one low-Al and Fe-rich sample (also showing a low $KAlO_2$ component) having Mg# 0.27. Apart from this sample, a rough trend of increasing Al characterizes the sequence from the biotite through the garnet–oligoclase to the andalusite–staurolite zones. High Al and Fe contents favour the formation of staurolite–andalusite-bearing assemblages, compatible with the formation of staurolite at low-*P* medium-grade conditions.

TEXTURAL RELATIONS AND MINERAL CHEMISTRY

Biotite zone

Psammo-pelites from this zone are composed of chlorite–muscovite–biotite–albite–oligoclase–quartz–ilmenite, and accessory graphite, apatite, ±rutile, tourmaline and zircon. These lithotypes are characterized by a penetrative S_2 foliation defined by phyllosilicates that transpose the S_1 foliation preserved within crenulation cleavage domains comprising muscovite–chlorite–quartz ± plagioclase ± ilmenite (Fig. 4a,b).

Biotite porphyroblasts (0.5 mm) are wrapped by muscovite and chlorite (Fig. 4a,b), indicating pre-S_2 growth. Locally, graphite inclusions within biotite

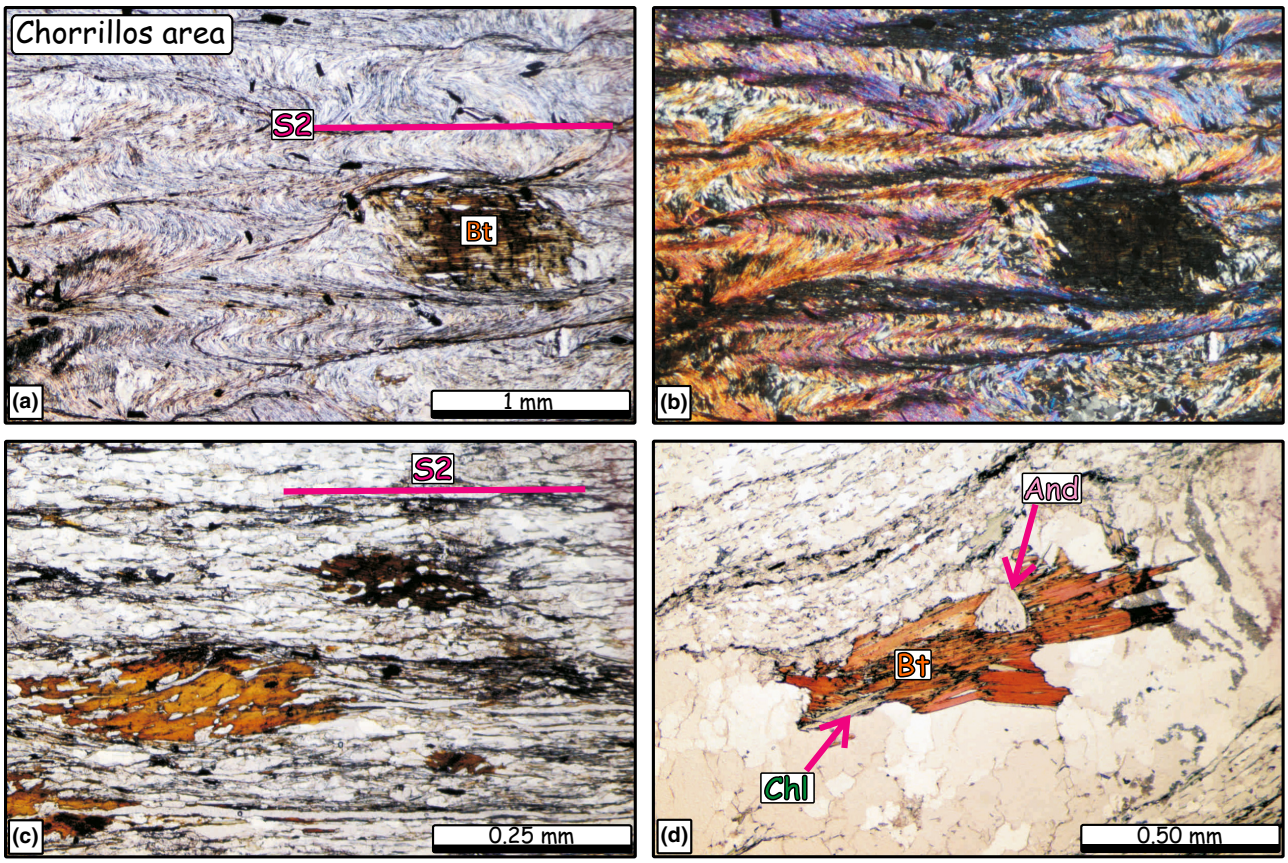

Fig. 4. Textural relations of biotite and garnet–oligoclase zone rocks in the Chorrillos area. (a) and (b) Pre-S_2 biotite porphyroblast wrapped by the transposition foliation S_2. (c) Sigmoidal biotite in psammo-pelite with S_2 as the main foliation. (d) Quartz vein with biotite and andalusite oriented parallel to the S_1 foliation.

define trails orthogonal to the external S_2 foliation, suggesting post-S_1 growth. Hence, we interpret D_1 as related to regional low-grade metamorphism (M1) predating the LP/HT metamorphism. In more strongly deformed samples, biotite lies parallel to the main S_2 foliation and also forms sigmoids that record the local development of ductile shear zones (Fig. 4c). Chlorite and muscovite form subhedral flakes and are usually inter-grown along thin layers in both S_1 and S_2 domains, intercalated with quartz–plagioclase layers. Ilmenite is the main oxide phase and occurs parallel to both S_1 and S_2. Local relicts of rutile within ilmenite cores are interpreted as vestiges of a previous M1 mineral assemblage formed before the LP/HT metamorphism. Retrograde chlorite replaces biotite porphyroblasts (Fig. 4a).

Muscovite has Si, Mg#, Ti and Na values in the ranges 3.05–3.15, 0.39–0.50, 0.01–0.05 and 0.07–0.14 a.p.f.u., respectively (Table S1a). In contrast to what is expected during an isobaric heating path (Chatterjee & Froese, 1975), muscovite in the biotite zone has lower Na contents than muscovite from medium-grade conditions (Fig. S3). One explanation for this pattern might be the lower Al content of bulk rock compositions from the biotite zone compared to those from higher grade zones (Fig. S2), favouring Si-rich (Na-poor) muscovite compositions. On other hand, the chemical zoning preserved within this group is irregular. Two samples have phengite compositions with Si contents of 3.23 and 3.28 a.p.f.u., which might represent relicts from the M1 metamorphism. Biotite shows minor chemical variability with Mg# in the range 0.37–0.41 and Ti contents of 0.09–0.12 a.p.f.u. (Table S1b). Chlorite has Mg# in the range 0.40–0.42, where the lower values represent retrograde compositions (Table S1c). Plagioclase grains yield distinct albite (Xab = 0.99) and oligoclase (Xab = 0.87–0.80) compositions (Table S1d) that we interpret as representing solvus phases of the peristerite gap. Ilmenite records minor chemical variability and is characterized by Fe^{2+}, Fe^{3+} and Mn contents of 0.94, 0.01 and 0.04 a.p.f.u., respectively.

Garnet–oligoclase zone

The lithotype in this zone comprises chlorite–muscovite–biotite–oligoclase–quartz–ilmenite and accessory garnet, graphite, apatite, tourmaline and zircon. When present, garnet is scarce (<1% mode). It forms subhedral to euhedral crystals (~0.25 to <1 mm in

diameter) with quartz, ilmenite and rare calcite inclusions. Biotite forms porphyroblasts (<1 mm in length). Chlorite–muscovite layers alternating with quartz–plagioclase layers defining the main S_2 foliation. Andalusite ± biotite occurs in quartz–plagioclase veins (Fig. 4d), which are folded by F_2. Muscovite has Si, Mg#, Ti and Na contents varying in the ranges 3.03–3.15, 0.36–0.53, 0.01–0.03, and 0.11–0.25 a.p.f.u., respectively (Table S1a). One analysis yielded Si = 3.34 a.p.f.u., and likely represents M1 mica. Biotite has Mg# in the range 0.35–0.40, and Ti contents in the range 0.08–0.12 a.p.f.u. (Table S1b). Chlorite records minor chemical variability and has Mg# in the range 0.37–0.42 (Table S1c). Garnet ($Xprp_{0.07}Xgrs_{0.04}Xalm_{0.74}Xsps_{0.16}$, Table S1e) is unzoned. Plagioclase is oligoclase in composition with Xab in the range of 0.77–0.87 (Table S1d). Ilmenite has Fe^{2+}, Fe^{3+} and Mn contents of 0.94, 0.02, and 0.04 a.p.f.u., respectively (Table S1f).

Staurolite–andalusite zone

Staurolite–andalusite-absent rocks

This lithotype comprises biotite–garnet–oligoclase/andesine–quartz–ilmenite with accessory graphite, epidote, apatite and tourmaline ± pyrite. The lack of muscovite, the predominance of plagioclase (~45%) and biotite (~23%), and low $KAlO_2$ contents (as indicated by the samples with lower Al contents in the AFM and AKF diagrams of Fig. S2) point to plagioclase-rich sedimentary protoliths. The rock fabric is characterized by a fine-grained matrix (0.01–0.15 mm), mainly formed of plagioclase with minor graphite, quartz and ilmenite. Graphite trails define the S_1 foliation together with granoblastic bands of plagioclase. Biotite, garnet and chlorite form post porphyroblasts (≤0.50, ≤0.50, and ≤1 mm, respectively). The continuity between inclusion trails defined by graphite, plagioclase and quartz in biotite grains and the matrix foliation is conspicuous and clearly identifies the growth as post-S_1. Biotite is partially resorbed, whereas garnet is euhedral. Compositional maps show two generations of garnet, of which garnet I is locally resorbed and replaced by garnet II to form atoll-like grains (Fig. 5). Chlorite occurs as porphyroblasts and as flakes within biotite along the cleavage or at the edges. This chlorite is aligned approximately with the hinges of the second crenulation foliation, indicating syn- to late-S_2 growth.

Biotite has irregular zoning but generally the inner zones have slightly lower Mg# (0.33) than the rims

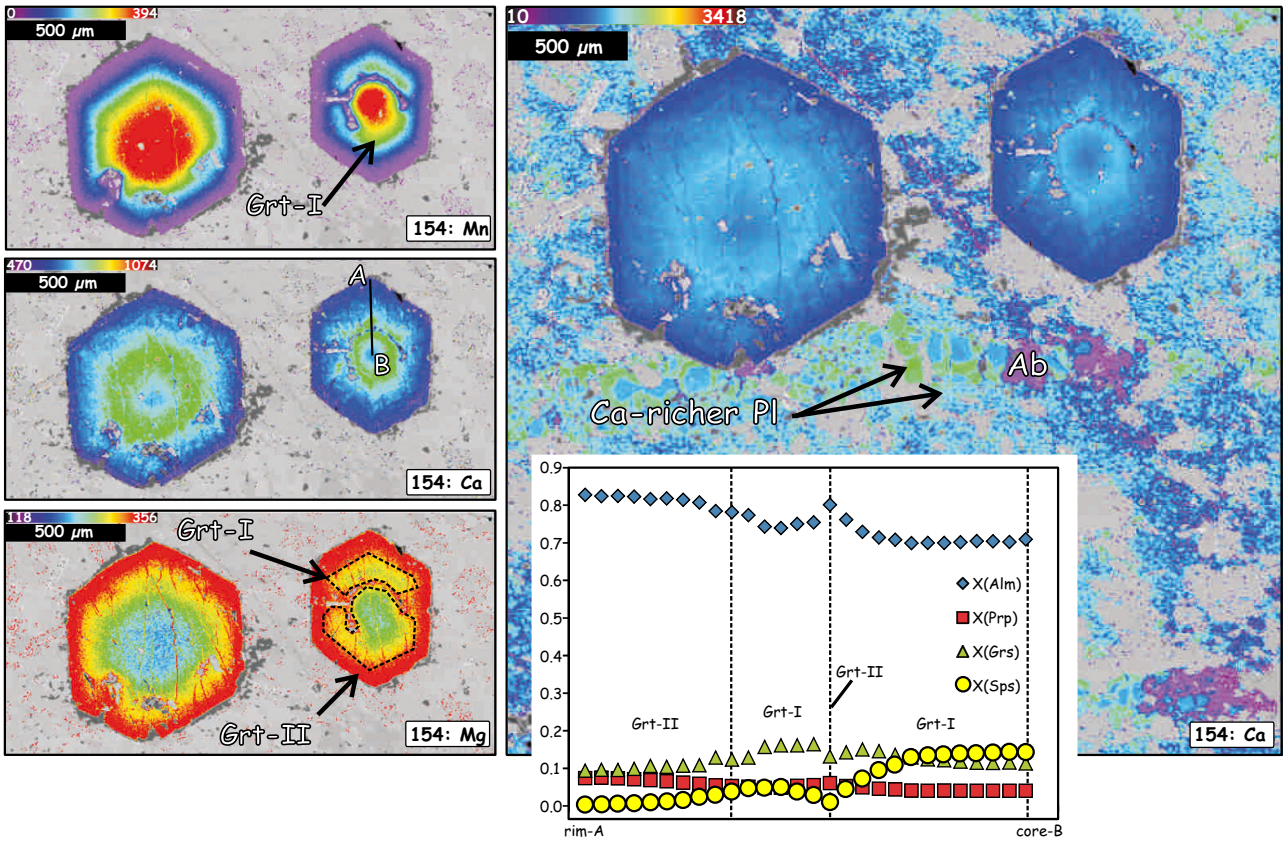

Fig. 5. Compositional images of garnet porphyroblasts and matrix plagioclase of psammo-pelite from the staurolite–andalusite zone (Tanumé beach). Colour scale bar (counts/nA/s) represents high (red) and low (purple) concentrations. See text for details.

(0.34 *v.* 0.37; Table S1b). Ti zoning is irregular, with contents varying in the range 0.06–0.13 a.p.f.u., but differences between cores and rims are not apparent. Ti-rich halos occur around ilmenite inclusions. Chlorite has Mg# in the range 0.37–0.39, with lower values at the rims (Table S1c). Ilmenite has Fe^{2+}, Fe^{3+} and Mn contents in the ranges of 0.92–0.98, 0.0–0.07 and 0.01–0.04 a.p.f.u., respectively (Table S1f). Epidote has Xcz and Xps contents of ~0.80 and ~0.20, respectively (Table S1f). Plagioclase is zoned (Fig. 5) with cores of oligoclase (Xab = 0.73–0.82) and rims of andesine (Xab = 0.58–0.60) (Table S1d). Late plagioclase is albite (Xab = 0.91–0.97) and concentrates along diffuse discordant strips that overprint/replace earlier plagioclase. In general, garnet porphyroblasts show prograde growth zoning characterized by decreasing Mn contents towards the rims (Table S1e), which is balanced by increasing Mg, Fe and Mg# ($Xprp_{0.03–0.09}Xgrs_{0.09–0.17}Xalm_{0.67–0.83}Xsps_{0.01–0.17}$ at the rims) (Fig. 5). However, as noted above, the growth–dissolution history of garnet is complex.

Prograde garnet zoning was affected by a stage of garnet resorption, which was followed by continued prograde growth (Fig. 5). Garnet I, which has higher Mn and Ca, and lower Mg and Fe than garnet II, comprises most of the grain (core and mantle). Garnet II forms inner and external overgrowths on garnet I and record peak conditions as indicated by the lowest Mn and highest Mg contents and highest Mg# (Fig. 5). Garnet I shows an annulus of higher Ca content (Xgrs = 0.11, 0.16, and 0.09 in the core, intermediate zone, and mantle, respectively), and flame-like features (cf. Pattison & Tinkham, 2009; and references therein) developed within the mantles (Fig. 5). The high Ca annulus is not accompanied by complementary changes in Mn, Mg and Mg#, suggesting kinetic effects likely involving other Ca-bearing phases (e.g. epidote and/or plagioclase as local sinks/sources for Ca) during prograde garnet growth rather than recurrences in *P–T* conditions (cf. Chernoff & Carlson, 1997). Compositional maps show Mg-rich and Mn-poor zones similar in composition to garnet II rims that invade garnet I from the rim (cf. Faryad *et al.*, 2010) that may follow the internal concentric zoning of garnet I and develop atoll-like structures (Fig. 5). This process involved the formation of minor biotite within the atoll, suggesting a dissolution–precipitation event of garnet I during formation of the garnet II rims. Finally, local minor resorption of garnet II rims by quartz did not involve diffusive modification of garnet compositions, indicating low-*T* retrograde conditions.

Staurolite–andalusite-bearing rocks

This lithotype comprises biotite–muscovite–chlorite–quartz–plagioclase ± staurolite ± andalusite–ilmenite with accessory graphite and tourmaline. Biotite (≤0.80 mm), staurolite (≤3 cm) and andalusite (up to several centimetres in length) form post-S_1 porphyroblasts, as evidenced by the continuity of inclusions trails (mostly muscovite, quartz and graphite) with the matrix (≤0.03 mm) mineral fabric (Fig. 6a), truncation of the inclusion fabric and wrapping by the S_2 foliation ($S_i \neq S_e$; Fig. 6b,c). Biotite has subidioblastic habit and occurs intergrown with andalusite (Fig. 6d) or forms stacks (Fig. 6b). Staurolite and andalusite occur in contact along rectilinear crystal faces indicating synchronous growth of all three porphyroblastic minerals prior to D_2 and formation of the S_2 foliation. Andalusite was also boudinaged and kinked during D_2. Andalusite-bearing quartz veins related to M2 are isoclinally folded by F_2 (Fig. 6e), defining the same structural relations with respect to S_2 as the porphyroblasts (Fig. 6c,d).

Staurolite has idioblastic habit, but shows minor resorption at its rims. Locally, it develops sector zoning (due to variations in Ti content). Staurolite forms poikiloblastic grains that may have inclusion-rich rims and inclusion-free cores, or that may show zonal concentration of inclusions (Fig. 6c), defining complex patterns with respect to the matrix foliation, and pressure shadows of quartz ± biotite ± chlorite parallel to S_2 (Fig. 6c). More rarely, poikiloblastic staurolite shows slightly crenulated quartz inclusions that lack continuity with the S_2 foliation ($S_i \neq S_e$), suggesting local weak deformation of S_1 prior to staurolite growth. Ilmenite included in staurolite was not affected by F_2 folds, whereas partially included ilmenite was deformed outside the porphyroblasts (e.g. Fig. 7).

Fine-grained muscovite defines the S_1 foliation. It is folded by F_2 and is included within post-S_1 porphyroblasts. Late muscovite and chlorite form flakes aligned with the S_2 crenulation cleavage (Fig. 6a,f) but also truncate S_2 (Fig. 6b). Muscovite fills necks of boudinaged andalusite and replaces it at the rims. Chlorite replaces biotite forming post-S_2 pseudomorphs. Such relations indicate syn-to late and post-S_2 growth of muscovite and chlorite.

Muscovite has Si, Ti and Na values varying in the range 3.02–3.12, 0.01–0.02 and 0.14–0.27 a.p.f.u., respectively (Table S1a), yielding the highest Na contents of all studied rocks, as indicated in Fig. S3 and in the AKF diagram of Fig. S2. The chemical zoning is irregular, but a negative correlation between higher Ti and lower Na is observed (Table S1a), suggesting a trend of increasing temperature (Chatterjee & Froese, 1975; Wu & Chen, 2015). Muscovite overgrowths on andalusite are characterized by Si, Mg# and Na contents of ~3.03, ~0.40 and 0.22–0.26 a.p.f.u., respectively. Biotite cores and rims have Mg# in the ranges 0.35–0.40 and 0.37–0.41, respectively (Table S1b). Chlorite has Mg# of 0.39–0.43, with lower values towards the rims (Table S1c). Staurolite zoning is faint. The rims and areas around ilmenite inclusions are richer in Ti (0.06–0.15 a.p.f.u.) as shown in compositional map of Fig. 7. A number of

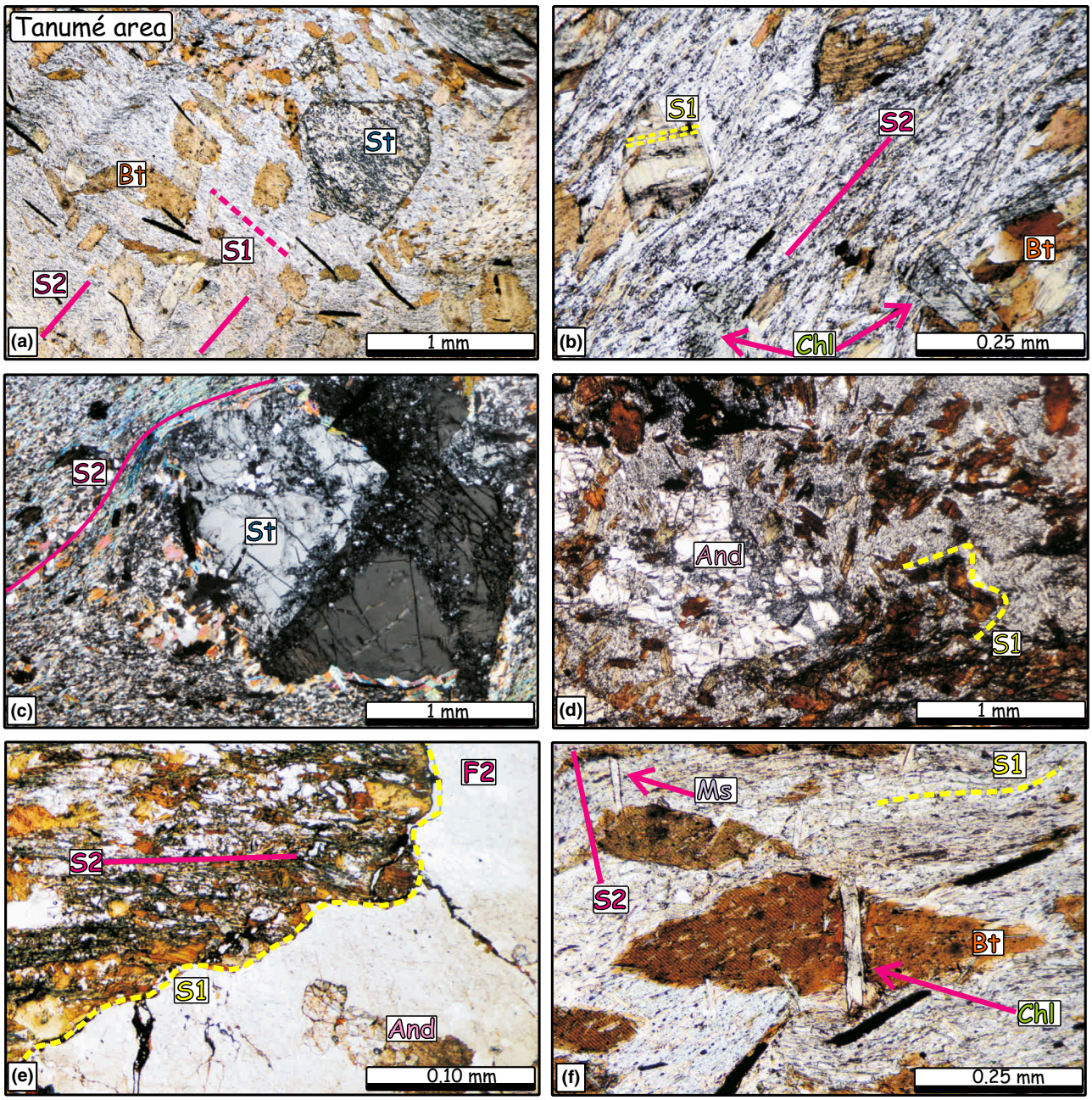

Fig. 6. Textural relations of staurolite–andalusite zone rocks at the Tanumé area. (a) Metapelite with post-S_1 biotite and staurolite. F_2 crenulation and S_2 spaced cleavage are shown. (b) Post-S_1 biotite forming stacks parallel to S_2; note inclusion trails of graphite oblique to the external foliation S_2, and post-S_2 chlorite. (c) Staurolite porphyroblast wrapped by S_2 with pressure shadow of quartz, muscovite and chlorite. Note zonal concentration of inclusions within staurolite. (d) S_2 wrapping around andalusite and rotated biotite marking the early foliation S_1. (e) Folded andalusite-bearing quartz vein. (f) Late-chlorite and muscovite flakes growing near parallel to the axial surface of F_2 crenulations.

staurolite grains have core and rim compositions characterized by Mg# = 0.12–0.14 and 0.15–0.16, and Ti = 0.05–0.08 and 0.08–0.16 a.p.f.u., respectively (Table S1g). The highest Ti values, however, occur around ilmenite inclusions. No chemical variations are observed between staurolite in different textural positions. Plagioclase is oligoclase in composition with Xab in the range 0.78–0.84 (Table S1d).

THERMODYNAMIC MODELLING

Pseudosections in the $MnO–Na_2O–CaO–K_2O–FeO–MgO–Al_2O_3–SiO_2–H_2O–TiO_2$ system

Pressure–temperature (P–T) pseudosections were calculated for three samples for which the peak phase relationships and whole-rock compositions are

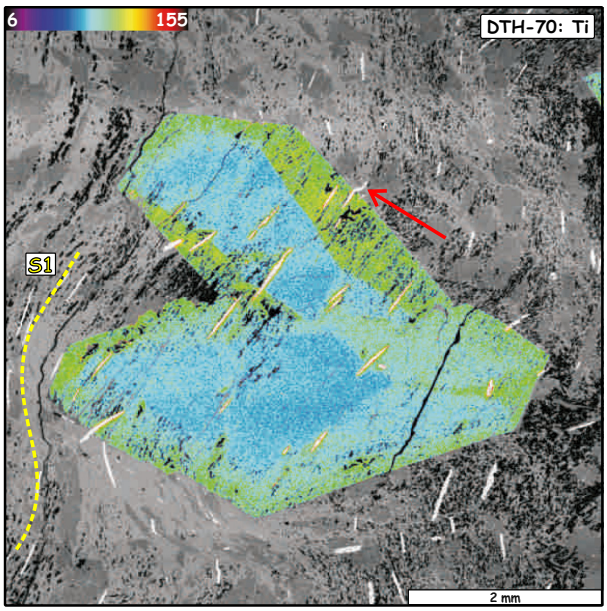

Fig. 7. Map of Ti concentration in twinned staurolite. Colour scale bar (counts/nA/s) represents high (red) and low (purple) concentrations. The red arrow indicates ilmenite deflection due to D_2. See text for details.

depicted in AFM diagrams projected from the coexisting phasese muscovite, quartz, plagioclase, ilmenite, apatite and H_2O fluid, and the exchange vectors $MnFe_{-1}$ and $SiNaAlCa_{-1}$ (Fig. S4**)**. The bulk composition of sample DTH-1C from the biotite zone plots on the tie-line biotite–chlorite. The bulk rock composition of sample DTH-68B from the transitional garnet–oligoclase zone plots within the tie-triangle chlorite–biotite–garnet. Note that projection from oligoclase and the plagioclase exchange vector makes Ca-bearing garnet plot with lower Al than chlorite (Fig. S4, DTH-68B). The bulk composition of sample DTH-69A from the staurolite–andalusite zone plots within the andalusite–staurolite–biotite tie-triangle (Fig. S4). These relations and the lack of tieline intersections suggest near-equilibrium of the respective assemblages in a continuous petrological–structural section at low to medium grade conditions.

Phase equilibria were calculated with the software package PERPLE_X (Connolly, 1990, 2005; version 6.6.8). The thermodynamic data used in the calculations are those of Holland & Powell (1998; revised in 2004, hp04ver.dat). The solution models of the solid phases chosen for the calculations include: garnet, potassic mica, staurolite, cordierite and ilmenite (Holland & Powell, 1998), plagioclase (Newton *et al.*, 1980), chlorite (Holland *et al.*, 1998), biotite (Powell & Holland, 1999; White *et al.*, 2000), and chloritoid (White *et al.*, 2000).

Due to the presence of graphite, the equilibrium composition of the fluid was treated as belonging to the C–O–H system (Ohmoto & Kerrick, 1977). Because dehydration reactions dominate in pelitic lithologies and the evolved H_2O typically allows perturbations in the fluid composition caused by addition of external fluids to be overcome (Connolly & Cesare, 1993), the H_2O, CO_2 and CH_4 contents of a C–O–H fluid coexisting with graphite (C), at fixed *P*–*T*, are those that satisfy the condition of maximum XH_2O in the fluid, i.e., the composition of the fluid must be located along the C–H_2O join of a C–O–H triangular diagram. This allows the fluid composition to be constrained to a fixed H:O ratio of 2:1 (Ohmoto & Kerrick, 1977; Labotka, 1991; Connolly & Cesare, 1993; Connolly, 1995), allowing the calculation of *P*–*T* pseudosections with varying but buffered fluid compositions.

Phase equilibria modelling was performed in the $MnO–Na_2O–CaO–K_2O–FeO–MgO–Al_2O_3–SiO_2–H_2O–TiO_2$ (MnNCKFMASHT) system. The CaO contents of the bulk compositions were corrected for apatite (assuming all P_2O_5 in apatite). Total iron was assumed as FeO_{total} and Fe^{3+} was not treated as a separate component, because fO_2 is low and controlled by equilibrium of graphite and fluid in graphite-bearing metapelites (Connolly & Cesare, 1993; Pattison, 2006). Samples with a low mode of porphyroblasts (<5%) were selected for thermodynamic modelling to diminish the effects of chemical fractionation during growth of zoned porphyroblasts (Marmo *et al.*, 2002; Konrad-Schmolke *et al.*, 2008). The *P*–*T* pseudosections were calculated in the range of 2–6 kbar and 350–650 °C with quartz and the fluid phase considered in excess. The calculated *P*–*T* diagrams include key isopleths of mineral composition and abundance that allow tracking the metamorphic evolution during both M1 and M2.

Biotite zone

In the pseudosection for sample DTH-1C (Fig. 8a), the peak mineral assemblage chlorite–biotite–oligoclase–albite–ilmenite–muscovite–quartz is represented by a quadrivariant field with a maximum pressure of ~4.5 kbar and temperature range of 450–500 °C. Using the Si and Na/Na+K contents of M2 muscovite (3.05–3.15 and 0.07–0.14 a.p.f.u., respectively), the *P*–*T* conditions are ~3.6 kbar at 485 °C. At <450 °C rutile is stable instead ilmenite, which is in accordance with observed relicts of rutile within ilmenite cores in this sample. The bulk composition is relatively Fe-rich and Al-poor (Figs S2 & S4) and, as expected, chlorite is stable over a wide *P*–*T* range up to ~500 °C, coexisting with staurolite within a very narrow field (trivariant field #11, Fig. 8a). Garnet is stable at pressures higher than ~4 kbar (>500 °C) or at low pressure at >550 °C, and andalusite–staurolite–biotite coexist in a quadrivariant field at >3.0 but <4.4 kbar, and at 500–550 °C (#10, Fig. 8a).

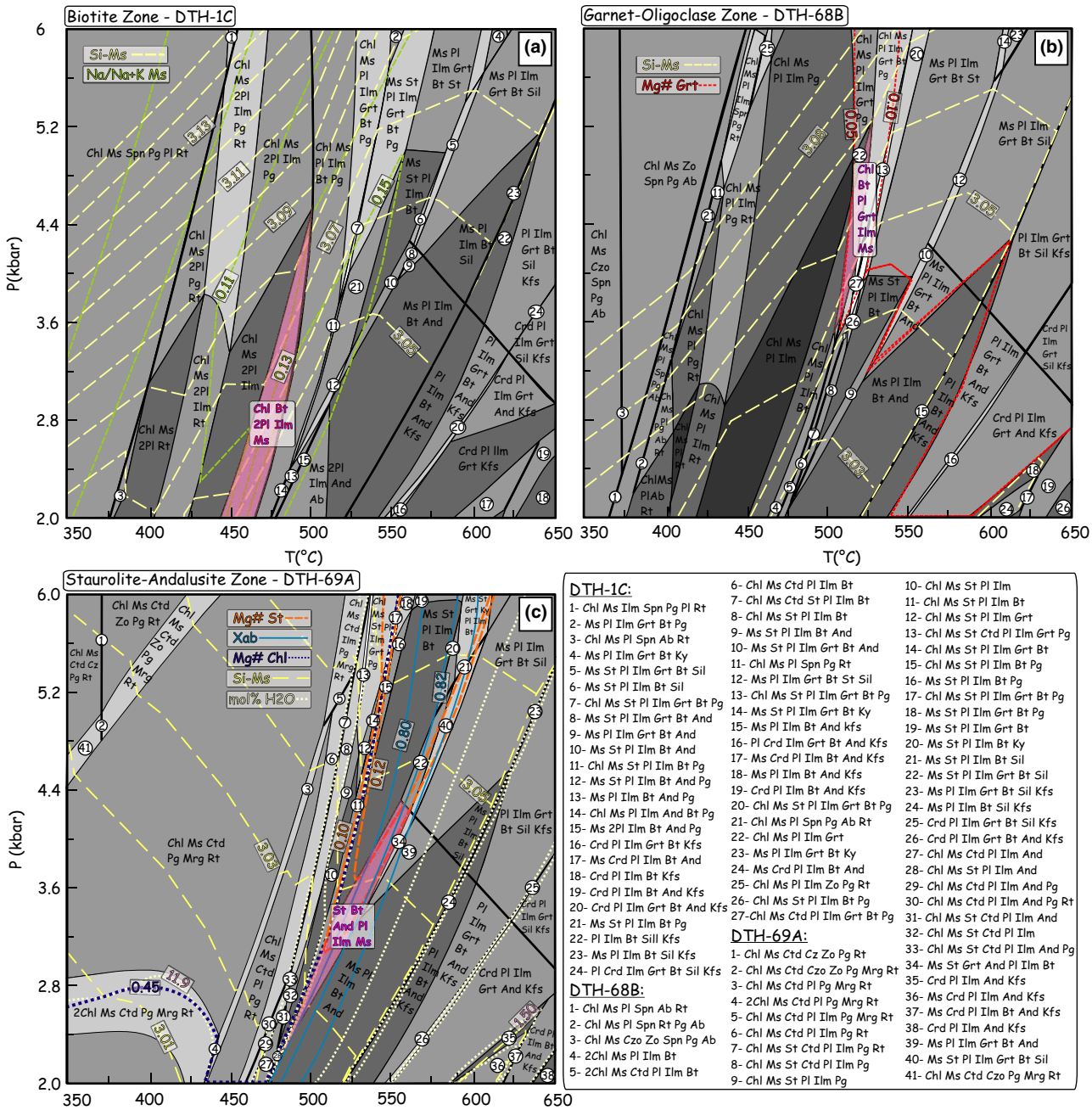

Fig. 8. *P–T* pseudosections for samples DTH-1C (a), DTH-68B (b) and DTH-69A (c) from the biotite, garnet–oligoclase and staurolite–andalusite zones, respectively. The highest variance ($F = 6$) is represented by the darkest gray tone and the lowest variance by white in narrow divariant fields. Pseudo-univariant and true univariant reactions are represented by thick lines (pseudo-univariant reactions separate fields with similar variance but with $F \neq 2$).

Garnet–oligoclase zone

In the pseudosection for sample DTH-68B (Fig. 8b), the peak assemblage chlorite–biotite–oligoclase–garnet–ilmenite–muscovite–quartz is represented by a quadrivariant field at 3.5–5.2 kbar and 500–525 °C. Combining chemical isopleths for the peak garnet rim Mg# (0.05) and Si contents in M2 muscovite (3.06 a.p.f.u.) constrains the peak *P–T* to ~4.4 kbar and ~515 °C (Fig. 8b). Garnet-bearing assemblages are restricted to slightly higher pressures at medium grade and low pressure at >525 °C, similar to Fig. 8a. Andalusite, staurolite and biotite coexist within a very narrow quadrivariant field (#9, Fig. 8b) extending from 485 to 550 °C over a wide pressure range of up to 3.8 kbar.

Staurolite–andalusite zone

In the pseudosection for sample DTH-69A (Fig. 8c), which is Al- and Fe-rich (Fig. S4), the peak assemblage staurolite–biotite–andalusite–oligoclase–ilmenite–muscovite–quartz is represented by a quadrivariant field from 2.4 to 4.3 kbar at 500–560 °C. There are minor differences between the analyzed Mg# in staurolite (0.12–0.16) and that predicted by thermodynamic modelling (0.10–0.14), but the Mg#-in-staurolite isopleth of 0.12 lies within the quadrivariant field of interest. Combining the compositional isopleths for staurolite (Mg# = 0.12) and plagioclase (Xab = 0.82) constrains *P–T* conditions to ~4.2 kbar at ~555 °C.

Ti in muscovite thermometer

For ilmenite- and Al_2SiO_5-bearing assemblages the Ti in muscovite thermometer (Wu & Chen, 2015) has been applied to samples from the staurolite–andalusite zone (DTH-69A, DTH-69C, DTH-70A). For a pressure of 4.2 kbar (Fig. 8c), using Ti-rich (0.02 a.p.f.u.) and Na-poor (0.14–0.20 a.p.f.u.) muscovite analyses (Table S1a) yielded 505 and 514 °C (Table S3). Considering an uncertainty of ±65 °C (Wu & Chen, 2015), these temperatures are comparable to those predicted from the *P–T* pseudosection (Fig. 8c). Retrograde conditions were also estimated using muscovite that replaces andalusite (Ti poorer, 0.01 a.p.f.u., and Na-richer, 0.22–0.25 a.p.f.u.). For a pressure of 2.8 kbar (retrograde chlorite isopleth of Mg# = 0.45; Fig. 8c), temperatures of 388–344 °C are obtained.

Ar–Ar AGES

Three samples were dated using the $^{40}Ar/^{39}Ar$ method, including one psammo-pelitic schist from the biotite zone in the Chorrillos area (DTH-1F, muscovite separates), one psammo-pelitic schist from the staurolite–andalusite zone in the Tanumé area (DTH-70A, biotite separate), and one blueschist from Infiernillo beach in the HP belt (see Fig. 2 for location and Willner, 2005 for the *P–T* conditions; DTH-86G, phengite separate). In all samples, two runs were performed using two to four grains per run (150–250 μm). Muscovite from sample DTH-1F yields plateau ages of 295.7 ± 1.6 Ma (MSWD = 1.65; 61.4% of ^{39}Ar released) and 294.9 ± 1.5 Ma (MSWD = 0.38; 72.0% of ^{39}Ar released) (Fig. 9a,b). For sample DTH-70A, plateau ages for biotite are 292.1 ± 1.6 Ma (MSWD = 1.52; 53.5% of ^{39}Ar released) and

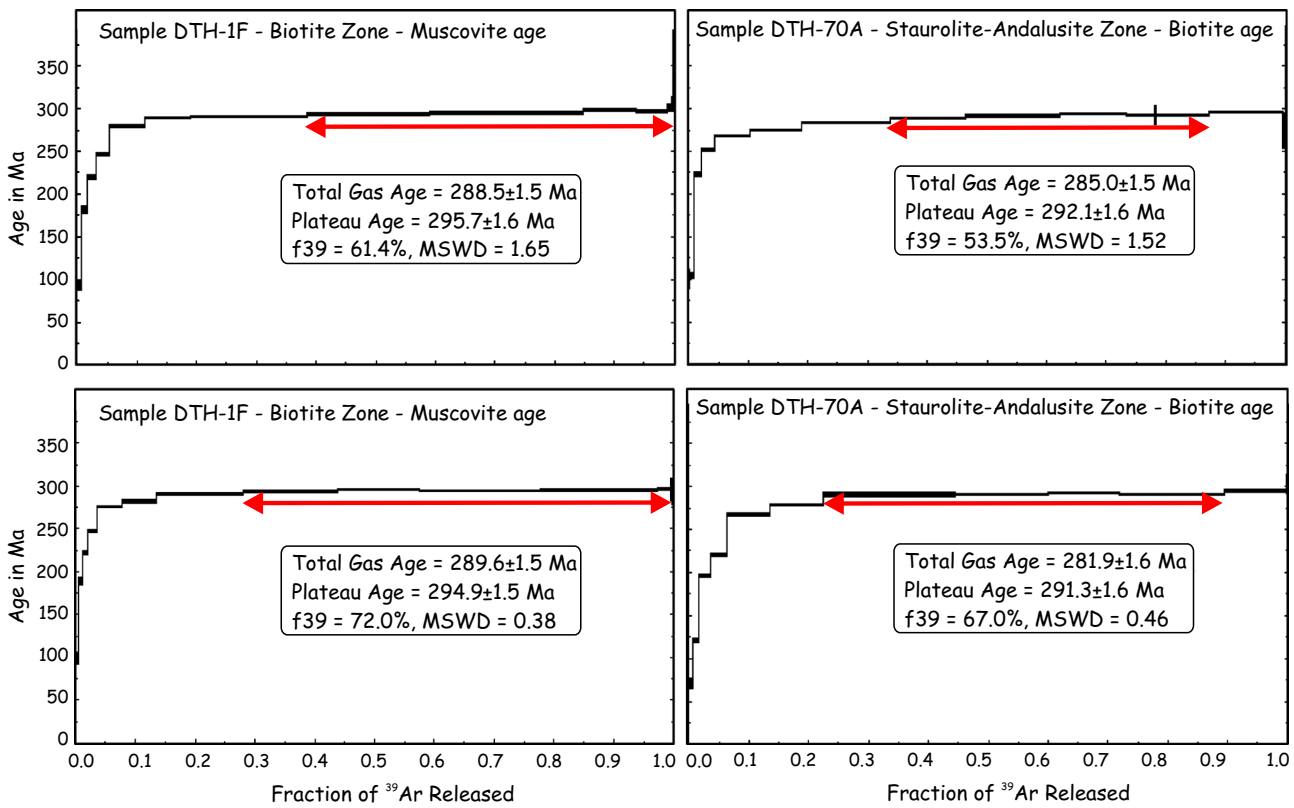

Fig. 9. Results of incremental step heating analysis of muscovite and biotite from samples DTH-1F (biotite zone) and DTH-70A (staurolite zone). See text for discussion.

291.3 ± 1.6 Ma (MSWD = 0.46; 67.0% of ^{39}Ar released) (Fig. 9c,d). Phengite from sample DTH-86G yields a plateau age of 299.6 ± 1.0 Ma (MSWD = 0.95; 85.6% of ^{39}Ar released) and a total gas age of 295.0 ± 0.9 Ma (Fig. S5).

To evaluate the geological meaning of these ages we adopt Ar closure temperatures for white mica and biotite of 420–350 °C and 300 ± 50 °C, respectively (McDougall & Harrison, 1999). Considering the temperatures calculated for the biotite (~450 °C) and andalusite–staurolite zones (~550 °C), we interpret the Ar muscovite and biotite ages to record cooling. However, for the blueschist sample, considering the peak conditions of 9.5–10.7 kbar and 350–385 °C estimated by Willner (2005), the Ar phengite ages are interpreted to record the timing of peak metamorphism.

DISCUSSION

The chemical-textural record and *P–T–t–d* paths

For the most part, metasedimentary rocks of the Eastern Series only record the effects of the thermal overprint, M2, that obliterated the textural and mineralogical records of the regional low-grade metamorphism, M1 (Hervé *et al.*, 1984; Willner, 2005). Combining field and microstructural data with thermodynamic modelling of the lower grade zones, we provide quantitative estimates of the *P–T* conditions and relative timing of the formation of the peak mineral assemblages. These data constrain the evolution of deformation within the central Chilean wedge and can be integrated with published geodynamic models.

The pressures determined for each zone based on intersecting compositional isopleths vary from 3.6 kbar in the biotite zone, to 4.4 kbar in the garnet–oligoclase zone and 4.2 kbar in the staurolite–andalusite zone. However, based on the mineral assemblage fields, the calculated pseudosections yielded consistent peak *P–T* estimates of 3.6–4.4 kbar at 485–555 °C across all three zones. Thus, it is unclear whether there are changes in depth from zone to zone, and the data are equally consistent with an isobaric thermal overprint. Although slightly higher-pressure estimates are obtained in this study, our results are comparable to those obtained by Willner (2005) for greenschist and amphibolite facies assemblages (2–3 kbar, 400–450 °C; 2.5–3 kbar 520–580 °C). The results are also in general agreement with the expected evolution of staurolite-bearing phase assemblages in metapelites from low-*P* thermal aureoles (Waters & Lovegrove, 2002; Pattison & Vogl, 2005; Pattison & Tinkham, 2009).

The formation of post-S_1 chiastolitic andalusite, staurolite and biotite assemblages (e.g. Figs 6, 8 & S4) reveals the static nature of the M2 metamorphism. The textural–mineralogical similarities between quartz veins bearing andalusite (±biotite) and the psammo-pelitic host rocks in the Tanumé and Chorrilos areas suggests that synmetamorphic veining with synchronous growth of andalusite in the vein and host rock (Cesare, 1994) occurred during the thermal metamorphism, as would be expected given the steep dP/dT slopes of the strongly temperature-sensitive isopleths of H_2O content in sample DTH-69A (staurolite–andalusite zone; Fig. 8c). This process involves coeval hydrofracturing and effective mass transport (intercrystalline diffusion and/or fluid-mediated) associated with andalusite-producing dehydration reactions, which allows the mobility of Al to form andalusite-bearing quartz veins (cf. Cesare, 1994 and references therein).

In addition, X-ray composition maps reveal evidence of local garnet dissolution followed by new growth (Fig. 5), i.e. during prograde metamorphism. Based on the textural relations and continuous prograde zoning evident in the garnet composition (Fig. 5), it is likely that the dissolution/growth process occurred close to peak *P–T* conditions during a single continuous metamorphic event. Hence we suggest that episodic infiltration of (relatively local or externally derived) fluid during prograde metamorphism triggered local dissolution of garnet-I while buffering the temperature. After the fluid infiltration event, garnet-II formed in response to increasing temperature in accordance with the observed prograde zoning (Fig. 5).

Isoclinal folding of andalusite porphyroblasts and andalusite-bearing quartz veins-bearing by F_2 folds (Figs 3d–f & 6e), wrapping and rotation of biotite, andalusite and staurolite porphyroblasts by the S_2 foliation (Figs 4a & 6c), and the presence of syn- to late-S_2 chlorite and muscovite indicate that D_2 deformation took place during cooling and exhumation (Fig. 10). Retrograde conditions estimated using samples from the staurolite–andalusite zone are compatible with decreasing temperature (<400 °C) associated with decreasing pressure (from 4.2 to 2.8 kbar).

Previous authors had proposed that porphyroblasts related to the thermal metamorphism were postkinematic with respect to both S_1 and S_2 foliations, and likely grew in the waning stages of the D_2 deformation (Willner, 2005; Willner *et al.*, 2009), implying that thermal metamorphism occurred after a change in the accretion mode in the accretionary prism. Here we have shown that andalusite, staurolite and biotite porphyroblast growth was post the S_1 and pre the S_2 fabric. However, we note that porphyroblasts grown late during D_1 or early during D_2 may exhibit similar microstructural relations making it difficult to distinguish between these alternative timing relations (cf. Passchier & Trouw, 2005). The connection between the new observations made here and the different deformational stages that prevailed in the wedge are discussed next in the context of changing mode of accretion.

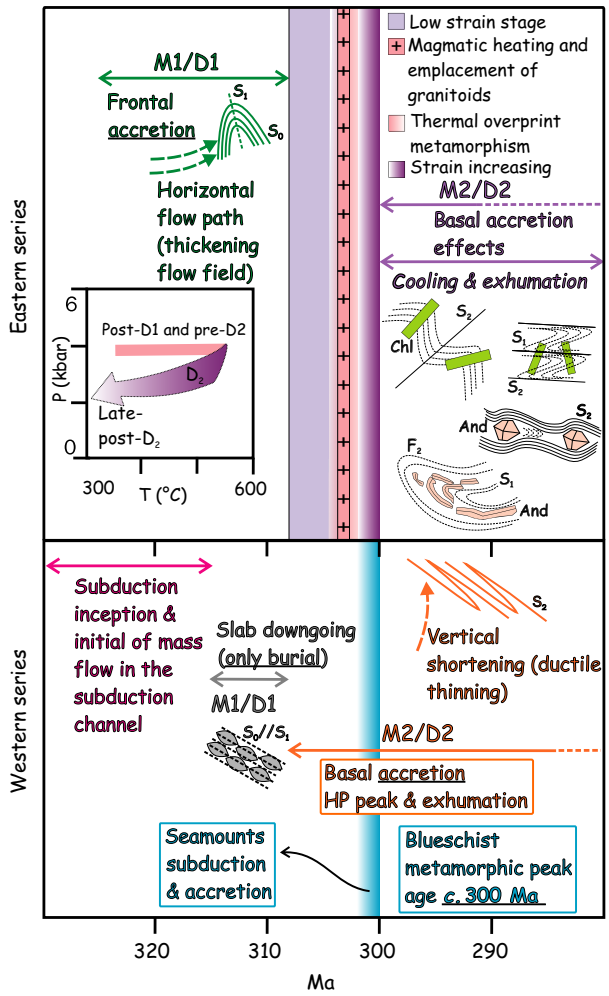

Fig. 10. Temporal relations between D_1 and D_2 deformations in both Western and Eastern series and geodynamic evolution of the accretionary wedge in the Pichilemu region (based on this study, Willner *et al.*, 2005; Richter *et al.*, 2007; Hyppolito *et al.*, 2014b). See text for discussion.

Timing relations and the development of the basal accretion-related foliation S_2

The revised microstructural relations and new metamorphic ages, combined with data from Willner *et al.* (2005) allow the tectonic evolution of both the HP/LT and LP/HT series to be correlated in this region. ^{40}Ar–^{39}Ar plateau ages of *c.* 300 Ma for muscovite (Willner *et al.*, 2005) and *c.* 292 Ma for biotite (this work) from staurolite–andalusite zone samples are interpreted to record cooling. Muscovite from the biotite zone samples yield near peak ^{40}Ar–^{39}Ar plateau ages of *c.* 295 Ma (this study). The blueschist sample from Infiernillo Beach yielded a ^{40}Ar–^{39}Ar plateau age of *c.* 300 Ma, interpreted to date the timing of the metamorphic peak, in general agreement with previous ^{40}Ar–^{39}Ar ages of *c.* 292 and *c.* 298 Ma retrieved from phengite by Willner *et al.* (2005) from blueschists samples from the Pichilemu region.

For a closure temperature of 300 ± 50 °C for biotite in the ^{40}Ar–^{39}Ar system, these result suggest that at *c.* 292 Ma the Eastern Series had likely cooled to a similar temperature to the high-*P* rocks forming the wedge, i.e. ~350 °C (Willner, 2005; Willner *et al.*, 2005), corroborating rapid cooling after the thermal overprint at *c.* 305 Ma, as was also suggested by Willner *et al.* (2005) based on the uniformity of muscovite cooling ages (*c.* 301–296 Ma). The close timing relation between blueschist facies metamorphism and the cooling stage for the LP/HT belt suggests a temporal correlation between basal accretion in the deeper part and cooling in the upper part of the wedge. Furthermore, we infer that formation of the S_2 foliation in the LP/HT belt was a consequence of basal accretion in the Pichilemu region at *c.* 300 Ma (Fig. 10).

The tectonic evolution of the accretionary prism

Richter *et al.* (2007) considered that only the deepest portion of the Eastern Series, at depths ~20 km where the S_2 foliation is locally developed, was affected by basal accretion. Our thermobarometric calculations, and structural and microstructural evidence indicates that the crust affected by the thermal metamorphism in the Pichilemu area was subsequently affected by the D_2 deformation at depths around ~11–16 km (this study; cf. Willner, 2005).

The proposed model for the tectonic evolution of the Central accretionary prism includes two different, successive and gradual modes of accretion (frontal and basal) driving the growth of the wedge (Richter *et al.*, 2007). Hyppolito *et al.* (2014a) showed that the subducting oceanic basin at the rear of the southwestern margin of Gondwana had a regional composite NMORB–EMORB–OIB pattern, and proposed that seamounts likely subducted episodically along the trench. Basal underplating started at *c.* 308 Ma, as documented by zircon dating of accreted sediments (Willner *et al.*, 2008), and corroborated by ^{40}Ar–^{39}Ar cooling ages for phengite from HP greenschists and the earliest subducted materials from the Western Series (Willner *et al.*, 2005, 2009, 2012; Hyppolito *et al.*, 2014b). Basal accretion preceded both the peak of blueschist metamorphism at *c.* 300 Ma in the Pichilemu region (Willner *et al.*, 2005) and cooling of the Eastern Series in the interval 301–292 Ma (Willner *et al.*, 2005; this study). These chronological relations and the interpretation that the blueschists represent accreted fragments of seamounts (Hyppolito *et al.*, 2014a) suggest a possible causal relationship between seamount subduction and the D_2 deformation at shallower levels of the accretionary wedge (Fig. 10).

After the D_1 deformation, shallower levels in the wedge behaved as a low strain zone, as indicated by

the static nature of the thermal overprint between the D_1 and D_2 deformations. Subsequently, shallower levels in the wedge were affected by the same deformation field as the deeper parts of the wedge, which suggests a high level of coupling between the subducting and overriding plates (cf. Richter *et al.*, 2007). This increased coupling may be explained by a seamount chain entering the subduction zone, which would have led to tectonic erosion (cf. Von Huene & Lallemand, 1990; Dominguez *et al.*, 1998; Ueda, 2005) and enhanced coupling by transferring material from the toe of the wedge to deeper in the subduction zone. In the Pichilemu region, the post-accretionary Pichilemu–Vichuquen fault juxtaposes different levels of the accretionary prism (Willner *et al.*, 2009), in contrast to the Maule region where Richter *et al.* (2007) described a continuous lithological and structural section between the Western and Eastern series. Thus, it is plausible that the variable effect of D_2 on shallow levels of the accretionary complex is a consequence of local and discrete perturbation in the subduction regime along this active plate margin, most likely related to the subduction of asperities on the incoming plate and their accretion at depth in the wedge.

CONCLUSIONS

Based on microstructural information, phase equilibria modelling and ^{40}Ar–^{39}Ar ages that enabled an integrated *P–T–t–d* analysis, we have shown that the shallower levels (~13 km depth) of the Palaeozoic accretionary prism in the Pichilemu region of the Chile margin were affected by a thermal overprint triggered by the intrusion of granites. The thermal overprint occurred after the frontal accretion-related D_1 deformation and likely before or early during the development of the penetrative S_2 foliation. The close temporal relation between the formation of blueschists in the adjacent HP/LT belt and cooling in the LP/HT belt at *c.* 300–292 Ma suggests that the subduction and accretion of topographic highs, now represented by the blueschists, enhanced coupling between downgoing and upper plates, favouring the development of the exhumation-related S_2 foliation at shallower levels in the wedge. This study demonstrates how mineral assemblages in paired metamorphic belts may record important information about the changing style of deformation within an accretionary system in circumstances where a direct microstructural and temporal correlation can be established between different levels in the wedge.

ACKNOWLEDGEMENTS

This work was supported by the São Paulo Research Foundation (FAPESP) Grant 2012/01191-1. The first author thanks FAPESP for scholarships 2012/17635-6 and 2010/11954-7 at the University of Granada and the University of São Paulo, F. Hervé (University of Chile) for sharing his knowledge of Chilean basement geology, and N. H. Carballo (Instituto Geológico y Minero de España), the collaborators of the TOR-ANDES project (CGL2012-38396-C03) and C. Palape (University of Chile) for fruitful discussion in the field. We acknowledge A. Willner, D. Pattison and J. Glodny for constructive reviews and improvements to a first version of this manuscript. M. Brown is fully acknowledged for careful revision and editorial handling.

REFERENCES

Aguirre, L., Hervé, F. & Godoy, E., 1972. Distribution of metamorphic facies in Chile – an outline. *Kristalinikum*, **9,** 7–19.

Angiboust, S., Glodny, J., Oncken, O. & Chopin, C., 2014. In search of transient subduction interfaces in the Dent Blanche-Sesia Tectonic System (W. Alps). *Lithos*, **205,** 298–321.

Berman, R.G., 1988. Internally-consistent thermodynamic data for minerals in the system Na_2O–K_2O–CaO–MgO–FeO–Fe_2O_3–Al_2O_3–SiO_2–TiO_2–H_2O–CO_2. *Journal of Petrology*, **29,** 445–522.

Brown, M., 2009. Metamorphic patterns in orogenic systems and the geological record. In: *Accretionary Orogens in Space and Time* (eds Cawood, P.A. & Kröner, A.), *Geological Society London Special Publications*, **318,** 37–74.

Brown, M., 2010. Paired metamorphic belts revisited. *Gondwana Research*, **18,** 46–54.

Brown, M., 2014. The contribution of metamorphic petrology to understanding lithosphere evolution and geodynamics. *Geoscience Frontiers*, **5,** 553–569.

Cesare, B., 1994. Synmetamorphic veining: origin of andalusite-bearing veins in the Vedrette di Ries contact aureole, Eastern Alps, Italy. *Journal of Metamorphic Geology*, **12,** 643–653.

Chatterjee, N.D. & Froese, E., 1975. A thermodynamic study of the pseudobinary join muscovite-paragonite in the system $KAlSi_3O_8$-$NaAlSi_3O_8$-Al_2O_3-SiO_2-H_2O. *American Mineralogist*, **60,** 985–993.

Chernoff, C.B. & Carlson, W.D., 1997. Disequilibrium for Ca during growth of pelitic garnet. *Journal of Metamorphic Geology*, **15,** 421–438.

Cloos, M., 1982. Flow mélanges: numerical modelling and geologic constraints on their origin in the Franciscan subduction complex. *Geological Society of America Bulletin*, **93,** 330–345.

Cloos, M. & Shreve, R.L., 1988. Subduction channel model of prism accretion, mélange formation, sediment subduction, and subduction erosion at convergent plate margins: 1. Background and description. *Pure and Applied Geophysics*, **128,** 455–500.

Connolly, J.A.D., 1990. Multivariable phase diagrams: an algorithm based on generalized thermodynamics. *American Journal of Sciences*, **290,** 666–718.

Connolly, J.A.D., 1995. Phase diagram methods for graphitic rocks and application to the system C-O–H–FeO–TiO_2–SiO_2. *Contributions to Mineralogy and Petrology*, **119,** 94–116.

Connolly, J.A.D., 2005. Computation of phase equilibria by linear programming: a tool for geodynamic modeling and its application to subduction zone decarbonation. *Earth and Planetary Science Letters*, **236,** 524–541.

Connolly, J.A.D. & Cesare, B., 1993. C–O–H–S fluid composition and oxygen fugacity in graphitic metapelites. *Journal of Metamorphic Geology*, **11,** 379–388.

Dominguez, S., Lallemand, S.E., Malavieille, J. & von Huene, R., 1998. Upper plate deformation associated with seamount subduction. *Tectonophysics*, **293,** 207–224.

Ernst, W.G., 1975. Systematics of large-scale tectonics age progressions in Alpine and Circum-Pacific blueschists belts. *Tectonophysics*, **26,** 229–246.

Faryad, S.W., Klápová, H. & Nosál, L., 2010. Mechanisms of formation of atoll garnet during high pressure metamorphism. *Mineralogical Magazine*, **74,** 111–126.

Feehan, J.G. & Brandon, M.T., 1999. Contribution of ductile flow to exhumation of low-temperature, high-pressure metamorphic rocks. San Juan-Cascade nappes, NW Washington state. *Journal of Geophysical Reasearch*, **104,** 10883–10902.

Gana, P. & Hervé, F., 1983. Geologia del basamento cristalino en la Cordillera de la Costa entre los rios Mataquito y Maule, VII region. *Revista Geologica de Chile*, **19–20**, 37–56.

Glodny, J., Lohrmann, J., Echtler, H. *et al*., 2005. Internal dynamics of a paleoaccretionary wedge: insights from combined isotope tectonochronology and sandbox modelling of the South-Central Chilean forearc. *Earth and Planetary Science Letters*, **231,** 23–39.

Glodny, J., Echtler, H., Figueroa, O. *et al*., 2006. Long-term geological evolution and mass flow balance of the South-Central Andes. In: *The Andes—Active Subduction Orogeny: Frontiers in Earth Sciences*, vol. 1 (eds Oncken, O., Chong, G., Franz, G., Giese, P., Götze, H.-J., Ramos, V., Strecker, M. & Wigger, P.), pp. 401–442. Springer-Verlag, Berlin.

Glodny, J., Echtler, H., Collao, S., Ardiles, M., Burón, P. & Figueroa, O., 2008. Differential Late Paleozoic active margin evolution in South-Central Chile (37° S–40° S) – the Lanalhue Fault Zone. *Journal of South American Earth Sciences*, **26,** 397–411.

González-Bonorino, F., 1971. Metamorphism of the crystalline basement of Central Chile. *Journal of Petrology*, **12,** 149–175.

González-Bonorino, F. & Aguirre, L., 1970. Metamorphic facies series of the crystalline basement of Chile. *GeologischeRundschau*, **59,** 979–993.

Gray, D.R. & Foster, D.A., 2004. $^{40}Ar/^{39}Ar$ thermochronologic constraints on deformation, metamorphism and cooling/exhumation of a Mesozoic accretionary wedge, Otago Schist, New Zealand. *Tectonophysics*, **385,** 181–210.

Greenwood, H.J., 1975. Thermodynamically valid projections of extensive phase relationships. *American Mineralogist*, **60,** 1–8.

Halama, R. & Konrad-Schmolke, M., 2015. Retrograde metasomatic effects on phase assemblages in an interlayered blueschist–greenschist sequence (Coastal Cordillera, Chile). *Lithos*, **216–217,** 31–47.

Hervé, F., 1977. Petrology of the crystalline basement of the Nahuelbuta mountains, southcentral Chile. In: *Comparative Studies on the Geology of the Circum-Pacific Orogenic Belt in Japan and Chile* (eds Ishikawa, T. & Aguirre, L.), pp. 1–51. Japan Society for the Promotion of Science, Tokyo.

Hervé, F., 1988. Late Paleozoic subduction and accretion in Southern Chile. *Episodes*, **11,** 183–188.

Hervé, F., Kawashita, K., Munizaga, F. & Bassei, M., 1984. Rb–Sr isotopic ages from late Paleozoic metamorphic rocks of central Chile. *Journal of the Geological Society of London*, **141,** 877–884.

Hervé, F., Calderón, M., Fanning, C.M., Pankhurst, R.J. & Godoy, E., 2013. Provenance variations in the Late Paleozoic accretionary complex of central Chile as indicated by detrital zircons. *Gondwana Research*, **23,** 1122–1135.

Hervé, F., Fanning, C.M., Calderón, M. & Mpodozois, C., 2014. Early Permian to Late Triassic batholiths of the Chilean Frontal Cordillera (28°–31°S): SHRIMP U-Pb zircon ages and Lu–Hf and O isotope systematics. *Lithos*, **184-187,** 436–446.

Holdaway, M.J., Mukhopadhyay, B., Dyar, M.D., Dutrow, B.L., Rumble, D. & Grambling, J.A., 1991. A new perspective on staurolite crystal chemistry: use of stoichiometric and chemical end-members for a mole fraction model. *American Mineralogist*, **76,** 1910–1919.

Holdaway, M.J., Mukhopadhyay, B. & Dutrow, B.L., 1995. Thermodynamic properties of stoichiometric staurolite $H_2Fe_4Al_{18}Si_8O_{48}$ and $H_6Fe_2Al_{18}Si_8O_{48}$. *American Mineralogist*, **80,** 520–533.

Holland, T.J.B. & Powell, R., 1998. An internally consistent thermodynamic data set for phases of petrological interest. *Journal of Metamorphic Geology*, **16,** 309–343.

Holland, T.J.B., Baker, J. & Powell, R., 1998. Mixing properties and activity–composition relationships of chlorites in the system $MgO–FeO–Al_2O_3–SiO_2–H_2O$. *European Journal of Mineralogy*, **10,** 395–406.

Hyppolito, T., Juliani, C., Garcia-Casco, A., Meira, T.V., Bustamante, A. & Hervé, F., 2014a. The nature of the Paleozoic oceanic basin at the southwestern margin of Gondwana and implications for the origin of the Chilenia terrane (Pichilemu region, central Chile). *International Geology Review*, **56,** 1097–1121.

Hyppolito, T., Garcia-Casco, A., Juliani, C., Meira, V.T. & Hall, C., 2014b. Late Paleozoic onset of subduction and exhumation at the western margin of Gondwana (Chilenia Terrane): counterclockwise P-T paths and timing of metamorphism of deep-seated garnet-mica schist and amphibolite of Punta Sirena, Coastal Accretionary Complex. *Lithos*, **216–217,** 409–434.

Isozaki, Y., 1996. Anatomy and genesis of a subduction-related orogen: a new view of geotectonic subdivision and evolution of the Japanese Islands. *The Island Arc*, **5,** 289–320.

Isozaki, Y., 1997. Contrasting two types of orogen in Permo-Triassic Japan: accretionary versus collisional. *The Island Arc*, **6,** 2–24.

Isozaki, Y., Aoki, K., Nakama, T. & Shuichi, Y., 2010. New insight into a subduction-related orogen: a reappraisal of the geotectonic framework and evolution of the Japanese Islands. *Gondwana Research*, **18,** 82–105.

Kato, T.T., 1985. Pre-Andean orogenesis in the Coast Ranges of Central Chile. *Geological Society of America Bulletin*, **96,** 918–924.

Kato, T.T. & Godoy, E., 1995. Petrogenesis and tectonic significance of Late Paleozoic coarse-crystalline blueschist and amphibolite boulders in the coastal range of Chile. *International Geology Review*, **37,** 992–1006.

Keane, S.D., Dewolf, C.P., Essene, E.J., Halliday, A.N., Hall, C.M. & Cosca, M.A., 2006. Isotopic constraints on the thermal history of the Wind River Range, Wyoming: implications for Archean metamorphism. *Canadian Journal of Earth Sciences*, **43,** 1511–1532.

Konrad-Schmolke, M., Handy, M.R., Babist, J. & O'Brien, P.J., 2008. Thermodynamic modelling of diffusion-controlled garnet growth. *Contributions to Mineralogy and Petrology*, **16,** 181–195.

Labotka, T.C. 1991. Chemical and physical properties of fluids. In: *Contact Metamorphism* (ed. Kerrick, D.), Reviews in Mineralogy, vol. 26, pp. 43–104. Mineralogical Society of America, Washington, DC.

Marmo, B.A., Clarke, G.L. & Powell, R., 2002. Fractionation of bulk rock composition due to porphyroblast growth: effects on eclogitefacies mineral equilibria, Pam Peninsula, New Caledonia. *Journal of Metamorphic Geology*, **20,** 151–165.

Martin, M.W., Kato, T., Rodriguez, C. *et al*., 1999. Evolution of the late paleozoic accretionary complex and overlying forearc-magmatic arc, south Central Chile (38–41S): constrains for the tectonic setting along the southernmost margin of Gondwana. *Tectonics*, **18,** 582–605.

Maruyama, S, 1997. Pacific-type orogeny revisited: Miyashiro-type orogeny proposed. *The Island Arc*, **6,** 91–120.

Maruyama, S., Masago, H., Katayama, I. *et al*., 2010. A new perspective on metamorphism and metamorphic belts. *Gondwana Research*, **18,** 106–137.

Massonne, H.-J. & Willner, A.P., 2008. Phase relations and dehydration behaviour of psammopelite and midocean ridge basalt at very-low-grade to low-grade metamorphic conditions. *European Journal of Mineralogy*, **20,** 867–879.
McDougall, I. & Harrison, T.M., 1999. *Geochronology and Thermochronology by the $^{40}Ar/^{39}Ar$ Method*. Oxford University Press, Oxford, 269 pp.
Miyashiro, A., 1961. Evolution of metamorphic belts. *Journal of Petrology*, **2,** 277–311.
Newton, R.C., Charlu, T.V. & Kleppa, O.J., 1980. Thermochemistry of the high structural state plagioclases. *Geochemica Cosmochimica Acta*, **44,** 933–941.
Ohmoto, H. & Kerrick, D.M., 1977. Devolatilization equilibria in graphitic schists. *American Journal of Science*, **277,** 1013–1044.
Passchier, C.W. & Trouw, R.A.J., 2005. *Microtectonics*. Springer, Berlin; New York, xvi, 366 pp.
Pattison, D.R.M., 2006. The fate of graphite in prograde metamorphism of pelites: an example from the Ballachulish aureole, Scotland. *Lithos*, **88,** 85–99.
Pattison, D.R.M. & Tinkham, K., 2009. Interplay between equilibrium and kinetics in prograde metamorphism of pelites: an example from the Nelson aureole, British Columbia. *Journal of Metamorphic and Geology*, **27,** 249–279.
Pattison, D.R.M. & Vogl, J.J., 2005. Contrasting sequences of metapelitic mineral-assemblages in the aureole of the tilted Nelson Batholith, British Columbia: implications for phase equilibria and pressure determination in andalusite-sillimanite type settings. *Canadian Mineralogist*, **43,** 51–88.
Platt, J.P., 1986. Dynamics of orogenic wedges and the uplift of high-pressure metamorphic rocks. *Geological Society of American Bulletin*, **97,** 1037–1053.
Platt, J.P., 1993. Exhumation of high-pressure rocks: a review of concepts and processes. *Terra Nova*, **5,** 119–133.
Powell, R. & Holland, T., 1999. Relating formulations of the thermodynamics of mineral solid solutions: activity modeling of pyroxenes, amphiboles, and micas. *American Mineralogist*, **84,** 1–14.
Richter, R.P., Ring, U., Willner, P.A. & Leiss, B., 2007. Structural contacts in subduction complexes and their tectonic significance: the Late Paleozoic coastal accretionary wedge of central Chile. *Journal of Geological Society London*, **164,** 203–214.
Ring, U. & Brandon, M.T., 1999. Ductile strain, coaxial deformation and mass loss in the Franciscan complex: implications for exhumation process in subduction zones. In: *Exhumation Processes: Normal Faulting, Ductile Flow and Erosion* (eds Ring, U. & Brandon, M.T.), *Geological Society London Special Publications*, **154,** 55–86.
Ring, U., Brandon, M.T., Willett, S. & Lister, G.S., 1999. Exhumation processes. In: *Exhumation Processes: Normal Faulting, Ductile Flow and Erosion* (eds Ring, U., Brandon, M.T., Lister, G.S. & Willett, S.), *Geological Society, London, Special Publications,* **154,** 1–27.
Spear, F.S. & Cheney, J.T., 1989. A petrogenetc grid for politic schists in the system SiO_2–Al_2O_3–FeO–MgO–K_2O–H_2O. *Contributions to Mineralogy and Petrology*, **101,** 149–164.
Streepey, M.A., van der Pluijm, B.A., Essene, E.J., Hall, C.M. & Magloughlin, J.F., 2000. Late Proterozoic (ca. 930 Ma) extension in eastern Laurentia. *Geological Society of America Bulletin*, **112,** 1522–1530.
Torres-Roldán, R.L., Garcia-Casco, A. & García-Sánchez, P.A., 2000. CSpace: an integrated workplace for the graphical and algebraic analysis of phase assemblages on 32-bit Wintel platforms. *Computers and Geosciences*, **26,** 779–793.
Ueda, H., 2005. Accretion and exhumation structures formed by deeply subducted seamounts in the Kamuikotan high-P/T Zone, Hokkaido, Japan. *Tectonics*, **24,** 1–17.
Von Huene, R. & Lallemand, S., 1990. Tectonic erosion along convergent margins. *Geological Society of America Bulletin*, **102,** 704–720.
Waters, D.J. & Lovegrove, D.P., 2002. Assessing the extent of disequilibrium and overstepping of prograde metamorphic reactions in metapelites from the Bushveld Complex aureole, South Africa. *Journal of Metamorphic Geology*, **20,** 135–149.
White, R.W., Powell, R., Holland, T.J.B. & Worley, B.A., 2000. The effect of TiO_2 and Fe_2O_3 on metapelitic assemblages at greenschist and amphibolite facies conditions: mineral equilibria calculations in the system K_2O–FeO–MgO–Al_2O_3–SiO_2–H_2O–TiO_2–Fe_2O_3. *Journal of Metamorphic Geology*, **18,** 497–511.
Whitney, D.L. & Evans, B.W., 2010. Abbreviations for names of rock-forming minerals. *American Mineralogist*, **95,** 185–187.
Willner, A.P., 2005. Pressure–temperature evolution of a Late Paleozoic paired metamorphic belt in North-Central Chile (34°–35° 30' S). *Journal of Petrology*, **46,** 1805–1833.
Willner, A.P., Hervé, F. & Massonne, H.-J., 2000. Mineral chemistry and pressure–temperature evolution of two contrasting highpressure–low-temperature belts in the Chonos Archipelago, Southern Chile. *Journal of Petrology*, **41,** 309–330.
Willner, A.P., Pawlig, S., Massonne, H-J. & Hervé, F., 2001. Metamorphic evolution of spessartine quartzites (coticules) in the high pressure-low temperature complex at Bahia Mansa Coastal Cordillera of South-Central Chile. *Canadian Mineralogist*, **39,** 1547–1569.
Willner, A.P., Glodny, J., Gerya, T.V., Godoy, E. & Massonne, H-J., 2004. A counterclockwise PTt path of high-pressure/low-temperature rocks from the Coastal Cordillera accretionary complex of south-central Chile. Constraints for the earliest stage of subduction mass flow. *Lithos*, **75,** 283–310.
Willner, A.P., Thomson, S.N., Kröner, A., Wartho, J.A., Wijbrans, J.R. & Hervé, F., 2005. Time markers for the evolution and exhumation history of a Late Paleozoic paired metamorphic belt in North-Central Chile (34°–35° 30' S). *Journal of Petrology*, **46,** 1835–1855.
Willner, A.P., Gerdes, A. & Massonne, H.-J., 2008. History of crustal growth and recycling at the Pacific convergent margin of South America at latitudes 29°–36° S revealed by a U-Pb and Lu–Hf isotope study of detrital zircon from late Paleozoic accretionary systems. *Chemical Geology*, **252,** 114–129.
Willner, A.P., Richter, P.P. & Ring, U., 2009. Structural overprint of a late Paleozoic accretionary system in north-central Chile (34°–35 °S) during post-accretional deformation. *Andean Geology*, **36,** 17–36.
Willner, A., Massonne, H.-J., Ring, U., Sudo, M. & Thomson, S.N., 2012. P-T evolution and timing of a late Palaeozoic fore-arc system and its heterogeneous Mesozoic overprint in north-central Chile (latitudes 31–32 °S). *Geological Magazine*, **149,** 177–207.
Wu, C.-M. & Chen, H.-X., 2015. Calibration of a Ti-in-muscovite geothermometer for ilmenite- and Al_2SiO_5-bearing metapelites. *Lithos*, **212–215,** 122–127.

SUPPORTING INFORMATION

Additional Supporting Information may be found in the online version of this article at the publisher's web site:

Figure S1. (a) Zone of intense foliation transposition; note the intrafolial quartz veins marking previous foliation S_1. (b) Andalusite porphyroblasts wrapped by S_2 foliation.

Figure S2. Bulk composition of metasedimentary rocks from the Chorrillos and Tanumé areas plotted

on AFM (left) and AKF (right, larger symbols) diagrams (projected from coexisting phases and appropriate compositional vectors, see text for explanation). The plotted end members of phases of interest include those relevant for the lower grade zones of the thermal overprint in the study area (Aguirre *et al.*, 1972; Willner, 2005; this work). The dashed circle in the biotite solid solution phase field shows the measured biotite composition (Table S1b). In the AKF diagram, muscovite compositions, which are represented by smaller symbols than whole rock compositions, are displaced towards A apex showing the influence of pyrophillitic ($K^{XII} + Al^{IV} = Y^{XII} + Si^{IV}$) substitution and/or a paragonite component.

Figure S3. Bivariant diagram showing chemical variation in white mica from the Chorrillos and Tanumé areas. There is a tendency for the Na content to increase as Si decreases from the low-Al pelites (biotite zone) to Al-richer pelites (staurolite–andalusite zone). See text for clarification.

Figure S4. AFM diagrams for selected samples from the biotite, garnet–oligoclase and staurolite–andalusite zones. The equilibrium mineral assemblages are indicated by the tie lines connecting mineral compositions. Bulk-rock compositions are also plotted. Olig., oligoclase.

Figure S5. Incremental step heating analysis of phengite of blueschist sample DTH-86G. See text for details.

Table S1. Mineral composition of samples from the Chorrillos (biotite and garnet–oligoclase zone) and Tanumé (staurolite–andalusite zone) areas.

Table S2. Bulk-rock composition of samples from the lower grade zones of the thermal overprint.

Table S3. Representative estimates of temperatures using the Ti-in-Ms thermometer for muscovite coexisting with ilmenite and Al_2SiO_5 polymorphs (Wu & Chen, 2015).

Received 21 August 2014; revision accepted 14 August 2015.